TÉCNICO LISBOA

Ring Based Zero-Field-Cooling YBCO Magnetic Bearing

Miguel Marques de Lima Roque

Thesis to obtain the Master of Science Degree in

Mechanical Engineering

Supervisors: Prof. Carlos Baptista Cardeira
Prof. Paulo José da Costa Branco

Examination Committee

Chairperson: Prof. Paulo Jorge Coelho Ramalho Oliveira
Supervisor: Prof. Paulo José da Costa Branco
Member of the Committee: Prof. João Murta Pina

November 2017

Dedicated to my family.

Acknowledgments

I would first like to express my gratitude to my thesis supervisors Prof. Carlos Cardeira, Prof. Paulo Branco and Prof. Rui Melício for all the support and availability throughout the time spent on this work and mainly for everything they taught me. Special thanks to Prof. Rui Melício for all the help regarding the organization and the writing of the document.

My sincere thanks to António Arsénio for all the help and all the amazing time spent working together to achieve our goals.

I would like to thank Sr. Raposeiro and Sr. Duarte for all the patience that they had helping me with the experimental setups and for their practical knowledge and help.

To all my lab mates, thanks for all the help and the good mood created. A special gratitude to Francisco for all the debated ideas, amazing help and team work.

I am extremely grateful to Joana, not only for reading my Master thesis and her very valuable comments, but also for all the support, amazing time spent and care expressed during all this time.

My gratitude to Fablab EDP for their help and availability to do the complex machinery involved in this work.

To my friends Tobias, António Henriques, Márcia, João Toipa, Aline e Pragana, thanks for facilitating the time working on our master thesis with good mood and happiness, even in difficult times.

Finally, special thanks to my mother, father and brother for all the support, education and the opportunity to fulfil the dream of studying in Instituto Superior Técnico, to all my family and friends, namely my flatmates for all the good moments spent throughout these six years.

Resumo

Esta tese incide na melhoria da configuração de um rolamento supercondutor que trabalha em levitação magnética. Os trabalhos desenvolvidos para tal fim são descritos nos parágrafos seguintes.

Desenvolveu-se uma configuração de um rotor com magnetos permanentes continuos ao invés de descontinuos no sentido de conseguir uma rotação mais estável e suave. A viabilidade desta concepção foi simulada e, posteriormente, testada utilizando um protótipo experimental.

Foi desenvolvido um modelo de elementos finitos para estudar a transmissão de energia no estator do protótipo do rolamento, através do qual foi analisado a taxa de evaporação de nitrogénio neste. Os resultados obtidos em simulação e experimentalmente foram comparados. Uma nova configuração foi ainda criada no sentido de minimizar esta taxa de evaporação.

Foi desenvolvida uma montagem experimental para acoplar o rolamento a um motor elétrico de forma a testar a rotação do rotor, no sentido de analisar o comportamento utilizando o rotor descontinuo e novo rotor continuo.

Foi elaborada uma montagem para acoplar um sensor de deslocamentos de alta resolução no sentido de analisar as vibrações e estabilidade do rolamento a funcionar.

O estudo do comportamento dinâmico do sistema axialmente e radialmente, respectivamente, foi também realizado.

Foi analisada a viabilidade do sistema, utilizando as duas técnicas de arrefecimento existentes: Field Cooling e Zero Field Cooling.

Este trabalho é a continuação de trabalhos anteriores que permitiram conceber com sucesso um rolamento rotativo sem atrito baseado em tecnologia supercondutora. Blocos supercondutores juntamente com ímanes permanentes são, hoje em dia, utilizados para criar sistemas de levitação, pois permitem configurações estáveis entre si e não exigem o uso de estabilizadores eletromagnéticos. O objetivo final deste projeto é usar esta tecnologia para criar um rolamento para máquinas elétricas.

Palavras-chave: Rolamento magnético superconductor; Zero Field Cooling; Supercondutores de alta temperatura; Magnetos permanentes de forma anelar; Levitação magnética; Rolamento para máquinas eléctricas

Abstract

This thesis focuses on improving the configuration of a superconducting bearing working magnetic levitation. The work developed for such purpose is described in the following paragraphs.

The configuration of a new rotor with continuous permanent magnets rather than discontinuous was developed in order to achieve a more stable and smooth rotation. The feasibility of this design was simulated and tested using an experimental prototype.

A finite element model was developed to study the energy transmission in the stator of the bearing prototype and the liquid nitrogen evaporation rate was analyzed. The results obtained in simulation and experimentally were compared. A new configuration has also been created in order to minimize this rate of evaporation.

An experimental assembly was developed to connect the bearing to an electric motor to test the rotation of the rotor in order to comapre the behaviour using the discontinuous rotor and new continuous rotor.

An assembly was developed to couple a high resolution sensor in order to analyze the bearing vibrations and stability in operation.

The study of the dynamic behaviour of the system axially and radially, respectively, was also performed.

The feasibility of the system using the two possible cooling techniques was analyzed: Field Cooling and Zero Field Cooling.

This work continues the previous work that allowed the successful design of a frictionless friction bearing based on superconducting technology. Superconducting bulks together with permanent magnets are nowadays used to create levitation systems, since they allow stable configurations among themselves and do not require the use of electromagnetic stabilizers. The main goal of this project is to use this technology to create a bearing for electric machines.

Keywords: Superconductor magnetic bearing; Zero Field Cooling, High temperature superconductor; Ring based permanent magnets; Magnetic levitation; Bearing for electrical machines

Contents

List of Tables

List of Figures

Nomenclature

Acronyms

FC	Field Cooling
FE	Finite Elements
FEM	Finite Elements Method
HTS	High Temperature Superconductor
PM	Permanent Magnet
SMB	Superconductor Magnetic Bearing
TC	Critical Temperature
YBCO	Yttrium Barium Copper Oxide
ZFC	Zero Field Cooling

Symbols

α	Thermal difussity
$\frac{\delta m}{\delta t}$	Liquid Nitrogen evaporation rate
μ	Magnetic permeability
μ_r	Relative magnetic permeability
ω_n	Natural frequency
τ	Time constant
υ	Kinematic viscosity
ζ	Damping ratio
B_t	Tangential component of magnetic flux density
F	Force
f_c	Fundamental frequency of signal from displacement sensor

f_c	Fundamental frquency of supply current
f_R	Rotor rotation frequency
F_S	Levitation force
h	Convection coefficient
h_e	Latent heat of evaporization
k	Heat conductance
L	Length
L_{opt}	Optimal length
M	Momentum
Nu	Nusselt number
Pr	Prandtl number
q	Heat trasnfer rate
Ra	Rayleigh number
s	Slip
T_f	Film temperature
T_n	Maxwell stress tensor
T_s	Surface temperature
T_∞	Room temperature
β	Expansion coefficient

Chapter 1

Introduction

The focus of this chapter is to introduce the most important topics required to a better understanding of the present work, explaining the motivations of the thesis. The organization of the document and the state of art are also addressed.

1.1 Background

The main objective of the present work is to develop a bearing based on superconducting technology. Thus, a theoretical introduction is made to provide detailed information about the required contents to understand it.

1.1.1 Superconductivity

Superconductivity is a phenomenon observed in several metals and ceramic materials in which the electrical resistance becomes approximately null and magnetic fields are repelled, when their temperature is lowered below the Critical Temperature (T_c), as explained in Fig. 1.1.

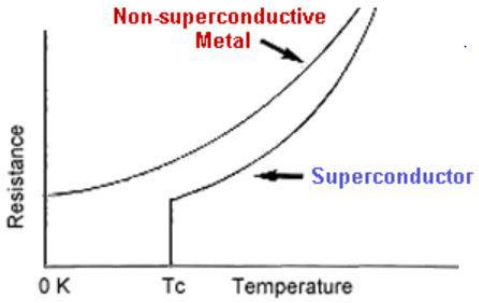

Figure 1.1: Superconductivity transition at TC [1].

It was firstly observed, when, in 1911, while cooling mercury to liquid helium temperatures (4.2 K), Kamerlingh Ohnnes found that the mercury at some temperature point, suddenly lost all of its electrical resistance. Quickly a number of other metals were discovered to possess the same interesting property.

This discovery created a great enthusiasm inside the scientific community with many believing that a method of conducting great amounts of energy with no losses in power had been found. It was soon realized through experimentation that these metals could not sustain very large currents [2].

In 1933, Meissner and Ochsenfeld discovered that in addition to losing all of its resistance, a superconductor expels all of its magnetic field from the superconducting interior [2]. In fact, the magnetic field does not penetrate into the superconductor, since the magnetic field inside is, by definition, the magnetic induction H, we can say that throughout a superconductor B = 0 [3]. See Fig. 1.2.

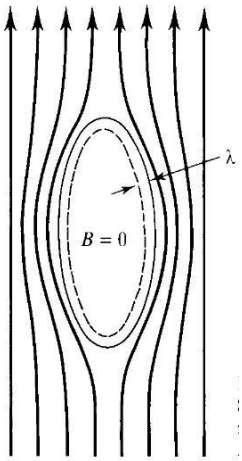

Figure 1.2: Schematic diagram of magnetic flux from interior of massive superconductor. [3].

This property holds the conditions under which the transition to superconducting state occurs. For example, if the metal is cooled in a magnetic field, then at the transition point the lines of magnetic force cease to enter the body [3].

In 1957 three American researchers - John Bardeen, Leon Cooper and John Schrieffer - established the microscopic theory of superconductivity. According to “BCS” theory, electrons group connect into pairs through interaction with vibrations of the lattice (so-called “phonons”), thus forming “Cooper pairs” which move around inside the solid without friction. The solid can be seen as a lattice of positive ions immersed in a cloud of electrons. As an electron passes through this lattice, the ions move slightly, attracted by the electron’s negative charge. This movement generates an electrically positive area which, in turn, attracts another electron. The energy of the electron interaction is quite weak and the pairs can be easily broken up by thermal energy – this is why superconductivity usually occurs at very low temperature [4].

In 1986 Bednorz and Müller have discovered a high-temperature superconductivity in layered materials dominated by cooper oxide planes [5]. Furthermore, the discovery of superconductivity in $YBa_2Cu_3O_7$ (YBCO) at 93 K by Chu’s group at Houston University and Maw Kwen Wu’s group at Huntsville University early 1987 brought down the liquid nitrogen temperature barrier of 77 K. [6]. This was a remarkable step, since liquid nitrogen is quite cheaper and it has easier access than the before mostly used liquid helium. Actually, materials of this sort have subsequently been discovered with T_c over 100 K. In Fig. 1.3 [7] is shown the chronological evolution of the TC for different materials.

Furthermore, the superconducting state can be destroyed by a rise of temperature or through a

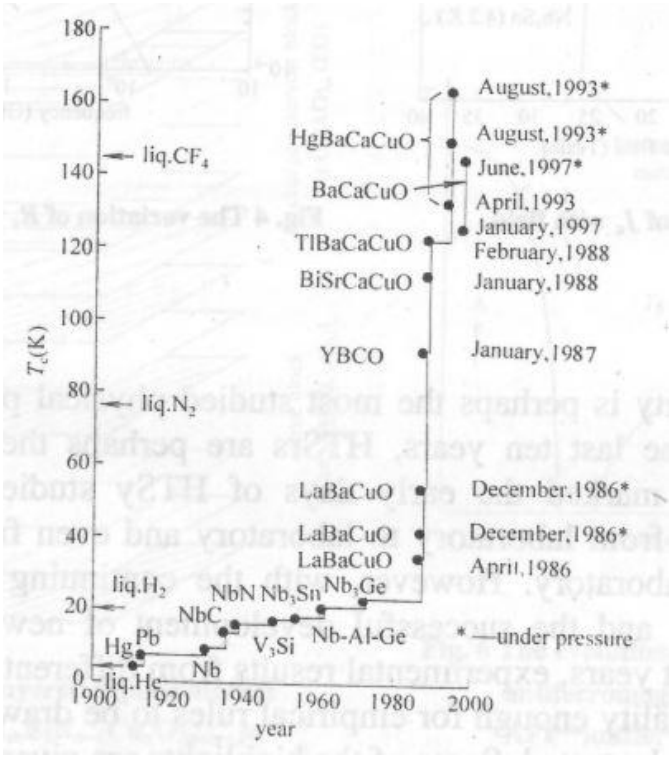

Figure 1.3: The evolution of TC with time [7].

magnetic field applied, which penetrates the material and suppresses the Meissner effect. In fact, a distinction is made between two types of superconductors. Type-I materials remain in the superconducting state only for relatively weak applied magnetic fields. Above a given threshold, the field abruptly penetrates into the material, shattering the superconducting state. On the other hand, Type-II superconductors tolerate local penetration of the magnetic field, which enables them to preserve their superconducting properties in the presence of intense applied magnetic fields [8]. YBCO is a type-II superconductor. Concerning this property type-II superconductor may be cooled by two different ways: Field Cooling (FC) is made in presence of magnetic field and Zero Field Cooling (ZFC) is made in the absence of magnetic field. They have some differences and both are actually used.

1.1.2 Bearings

A bearing is a component that constrains motion to a desired direction, also trying to reduce friction between mobile parts. More specifically, rotary bearings hold the position and weight of rotating components such as shafts or axles from the source of the load to the structure supporting it and allowing rotation[9]. These mechanical components are found in the most of the mechanical systems , since a simple ceiling fan until a aiplane or a refrigerator [10]. Fig. 1.4 shows a common mechanical ball bearing.

Figure 1.4: Mechanical ball bearing [9].

Mechanical Bearings

Bearings have played an important role since their invention and from the first industrial revolution the utilization of these components in mechanical systems and machines has widely spread. However, the most conventional bearing, i.e. mechanical bearings, reveal some disadvantages, mainly due to existing friction between the bearing and the bearing support. Problems as wear, cracks and energy losses (Fig. 1.5) are associated with this component.

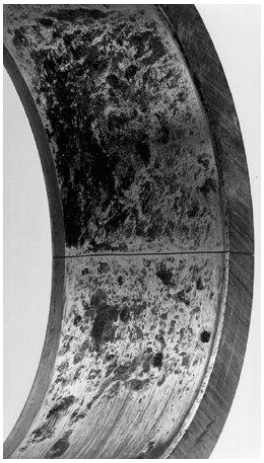

(a) Damaged bearing due to wear [11]

(b) Cracked bearing [11]

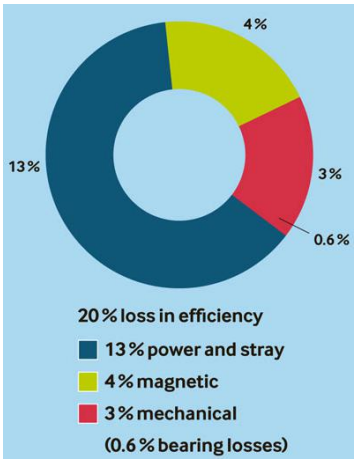

(c) Loss energy in a eletrical machine [12]

Figure 1.5: Most usual problems associated to mechanical bearings.

Magnetic Bearings

In the 1980s magnetic bearing systems became magnetic bearings became enabling technologies for flywheels [13] and since then, mechanical bearings have been replaced by magnetic bearings in specific applications and environments. In fact, magnetic bearings reveal benefits for rotating components to

work in high speed, high power and without mechanical contact or friction [14]. Furthermore, since these components do not require any lubricant they can be used in vacuum and in very clean environments.

In spite of that, magnetic bearings have also some limitations. Earnshaw's theorem states that paramagnetic materials, i.e. with relative magnetic permeability greater than one, cannot be in a stable equilibrium under electrostatic, magnetostatic and gravitational forces exerted by a stationary system [15], which forbids magnetic levitation in many common situations. Thus, bearings using only usual permanent magnets (PM) cannot produce a stable state. Moreover, bearings based on electromagnets (active magnetic bearings) require a current supply to make the control adjustments to balance the applied load.

Superconductor Bearing

Diamagnetic materials, i.e. with a relative permeability less than one, and superconducting materials permit stable configurations [15].

Thus, the best performing magnetic bearings in terms of passive stability are the high-temperature superconducting magnetic bearing (SMB), which can levitate flywheel automatically without need of electricity or positioning control system. However, HTS magnets require cryogenic cooling by liquid nitrogen [16].

1.2 Motivations

When compared with mechanical bearings, magnetic bearings reveal benefits, mainly since they work with no contact, which allows:

1. to have absence of friction;
2. to achieve higher angular velocities;
3. to work with low maintenance and very high life time expectancy.

The mixed state of that the type-II superconductors under the he influence of an external magnetic field allows a SMB to keep a shaft in a stable position by levitation and also counterbalances radial and lateral forces. Furthermore, a SMB does not require electromagnetic regulation to make control adjustments. Hence, a SMB using both HTS and PM may operate successfully as a passive magnetic bearing.

Thus, Superconductor Magnetic Bearings are:

4. passive Magnetic Bearings with no need of power supply;
5. self-centering rotational bearings due to the intrinsic damping;
6. wear-free and vacuum-compatible operation [17];
7. radial-type SMB in particular, is compact and robust in design, suitable for supporting high loads [17].

Regarding the cooling procedure, the ZFC reveals some advantages when compared with the field cooling technique, because FC implies significant hysteresis losses due to the magnetic flux trapping [18]. Furthermore, for horizontal SMB, previous studies showed that Zero Field Cooling provides effective lateral stability and higher levitation forces than the commonly used Field Cooling [19].

Hence, in this thesis the development of a horizontal frictionless SMB, is proposed to create a better alternative to replace the conventional mechanical and magnetic bearings.

1.3 State of Art

Concerning levitation systems, permanent magnets alone cannot produce a stable state. Hence, most of such systems uses type II superconductor bulks, besides permanent magnets. In this section, the most recent levitation bearings using these two components are mentioned. Not only, SMB developed in academic context are analyzed, but also existing products are taken into account.

This work follows the ideas and strategies developed in [1, 18, 19, 20]. Hence, the legacy work will be briefly explained to provide the reader a better understanding.

1.3.1 Research

In [21] a passive Superconducting Magnetic Bearing was analysed to create a more effective twist element in the textile technological process of ring spinning, since frictional wear and heat are the limiting factors for productivity of such devices.

In [22] a multi-surface levitation concept using three PMs and one HTS was studied for different configurations to reach the highest possible levitation forces, in order to maximize the stiffness of a mechanical flywheel system. An increase of 44.25% was achieved in the levitation force of three surface case with attractive PM.

In [23] a vertical superconductor bearing with the superconductor bulk as the rotating part was tested using ZFC and FC. The results of both techniques were compared, concerning axial forces, axial stiffness and their characteristics. In ZFC tests, the maximum levitation force, i.e. the axial force, was around one-third of the observed in FC.

In [24] a flywheel energy storage system at 100-kW level was developed and tested. The design conception and test up to 6000 rpm are presented.

Other authors have deeply studied important features of different SMBs, namely a dynamical stiffness model in [25] and the effect of the magnetic configuration on the rotational motion in [26].

1.3.2 Products

In 2006, after severall years of research, Siemens and Nexans presented the first superconductor bearing for industrial applications [27]. The stator is made of Cu half shells with 270 YBCO monoliths and the rotor is assembled from neodymium (NdFeB) ring segments. The components and the assembly may be seen in Fig. 1.6. This radial bearing has capacity of 5 kN under static and rotating conditions, vertical stiffness at a stator temperature of 28 K of 5.1 kN/mm, linear force-displacement over 0.3 mm displacement range. The oscillations of the shaft at the nominal operational speed of 3600 rpm are small.

Evico, a manufacturer of materials, technical components and systems in the field of high-temperature superconductivity, has developed industrial rotating and linear bearings aimed for vacuum and clean-room applications [28]. The bearings can be designed as cylindrical, planar and conical bearings as conventional mechanical bearings. The air gap, bearing force and bearing-stiffness can be adjusted ac-

(a) bearing cryostat

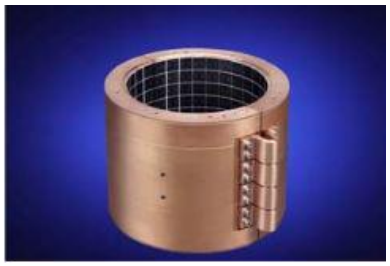

(b) Stator with YBCO shaped parts

(c) Assembled SMB

Figure 1.6: SMB for industrial applications developed by Siemens and Nexans [27].

cording to the application. The evico SMB specifications for a cylindrical rotating bearing are presented in Table 1.1.

Table 1.1: evico SMB specifications [28].

	Axial	Radial
Bearing Force	$>$5000 N	1000 N
Bearing Stiffness	2000 N/mm	1200 N/mm
Air-gap	1.5 mm	-
HTS-area	402 cm^2	-
Dimensions	ø 200 x 120 mm	-

CAN superconductors Company, the leading European manufacturer of HTC superconducting bulk materials, in cooperation with MAGSOAR, a German-Spanish company, offer bearings, based on superconductivity technology, able to reach very high speeds with high stiffness and load capabilities [29]. Further technical data are:

- Temperature: from 90 K to 4 K;
- Load capability: up to 100 kg;
- Speeds: up to 60 000 rpm;
- Specific stiffness: up to 500 N/mm.kg;
- Maintenace free, very low outgassing.

1.3.3 Legacy Work

In previous works, our research team achieved reliable results using superconductor technology to study and create levitation systems, namely a new Maglev design using ZFC YBCO superconductors [30, 31], among others. Following similar concepts and strategies, the ZFC YBCO Magnetic bearing has been developed [19, 18, 20], using PMs. Lately, levitating systems use these two components and regarding to levitating bearings and flywheels, their application has been increasingly spread. The ZFC SMB is composed of a fixed part (stator) and a rotating and levitating part (rotor), as shown in Fig. 1.7.

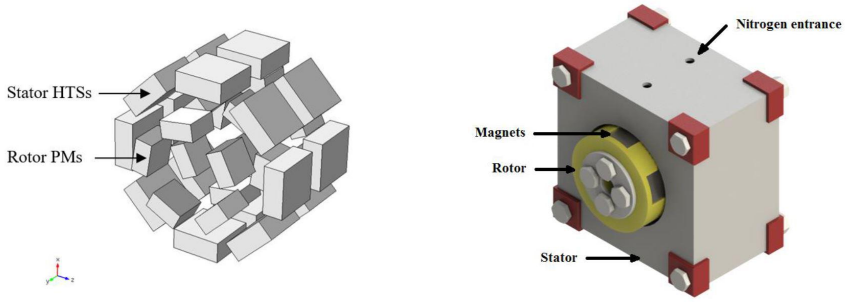

(a) SMB design (b) Final assembly view

Figure 1.7: Legated SMB design [20]

.

The stator contains two discontinuous rings of sixteen equally spaced bulk YBCO superconductors. This part was specially developed to fill with liquid nitrogen, in order to cool the HTS bulks. An exhaustive work about isolation of the structure was done, in order to reach low liquid nitrogen consumption and it is described in [32].

The rotor part contains three discontinuous rings with five equally spaced NdFeB permanent magnets each one. The three inner discontinuous rings of PMs are magnetized in alternate North-South-North way, such as the two border rings of magnets have concordant polarizations and the middle ring of magnets opposite polarization [19]. Due to budget limitations, only six superconductors were used on the bottom of the stator in the prototype version. A representative drawback of the superconductor bulks position is shown in Fig. 1.8 (c). The real prototype developed is presented in Fig. 1.8 (d).

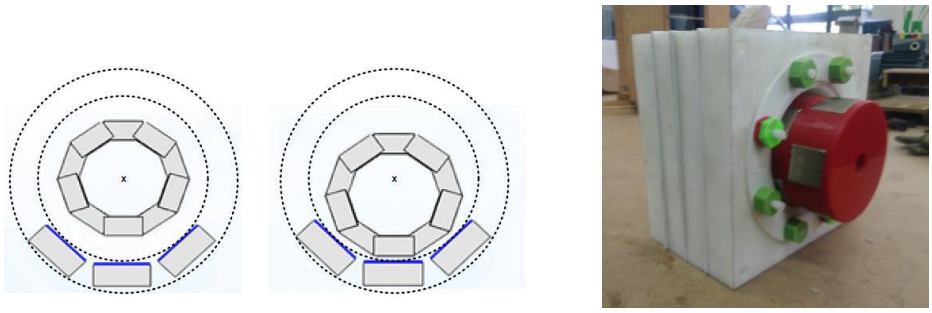

(a) Superconductor bulks disposition in the real prototype stator. Rotor and Stator concentric and misaglined, repectively

(b) Real prototype

Figure 1.8: SMB prototype [20]

.

Further and more detailed information about the structure and properties of the SMB may be consulted in [1].

1.4 Objectives/Contributions

The main objective of the present work is to develop the legated horizontal ZFC SMB, in order to replace the conventional mechanical bearing in electrical machines.

For this purpose, ring PMs were purchased to create a bearing with smoother rotation. Several analysis are going to be proceeded to compare the differences and understand the benefits of using ring based PMs rotor, instead of the bulks based PMs rotor.

An important goal of our research team is to evaluate the operation of the SMB replacing a mechanical bearing of an electrical machine. Therefore, a setup is required to be prepared to adapt the SMB to such function.

The biggest disadvantage of SMB is the dependence of liquid nitrogen utilization to cool the HTS bulks, which easily evaporates. The stator is thermally studied, in order to improve the isolation and decrease the requirement of high quantities of it.

Moreover, the dynamics and stability of the system are going to be matter of study.

1.5 Publications

When working in an original investigation subject where the objective is to contribute for the scientific and technological development, it is fundamental that the results are periodically published to incentive the discussion and sharing of ideas in the scientific community, with the intuit of achieving scientific and technological improvement. Subsequently, the sections with the scientific publications in international conferences are presented with all the details of their contribution for this thesis.

The following publication was an outcome from the works described on this thesis and presented in EUCAS 2017, a worlwide forum where the most recent advances in all areas of applied superconductivity:

- Paper in journal: A.J. Arsénio, M. Roque, M.V. Carvalho, C. Cardeira, R. Melício, P.J. Costa Branco, ”Implementation of a YBCO superconducting ZFC-magnetic bearing prototype”, IEEE Industry Application Magazine, pp. 1–9, 21 November 2017.

- Paper in International conference: A.J. Arsenio, M. Roque, C. Cardeira, R. Melício, P.J. Costa Branco, ”Prototype of a rings based zero-field-cooled (ZFC) YBCO magnetic bearing”, 16th European Conference on Applied Superconductivity-EUCAS2017, Geneva, Switzerland, 17–22 September 2017.

1.6 Thesis Outline

For a better understanding of the thesis, the description of the document is explained in this section. The implementation of the work is divided in two main Chapters. The conclusions and suggestions for future work are described in the final Chapter. The document structure is the following:

- Chapter 2 - Simulations and Viability. Some theoretical models are described, namely Levitation force prediction, in order to understand the viability of the new SMB based in a continuous rotor, and a stator thermal analysis. This Chapter also describes the conception work of components and setups using a 3D CAD Design Software.
- Chapter 3 - Experimental Part and Results. All the experimental methodology is described and the results are debated. Several analyses about different important characteristics of the SMB are going to be analysed.
- Chapter 4 - Conclusions and Future Work. The more significant achievements are referred and their importance is explained. In addition, ideas that might improve the SMB are described.

Chapter 2

Simulations

In this chapter, several analysis are made based on FEM, in order to evaluate new approaches to improve the legated SMB. The two biggest disadvantages observed before were the unstable rotation of the SMB, due to the discontinuous PM and HTS design, and the fast liquid nitrogen evaporation rate. Therefore, the viability of a new rings based PMs rotor and a stator thermal analysis are going to be debated for the purpose of reducing such problems. Furthermore, the conception of the new rotor and a setup to evaluate the SMB operation as a bearing for electrical machines are going to be explained.

2.1 Rings Based Rotor - Viability and Conception

In [1, 18, 20, 19] a SMB constituted by one rotor with discontinuous PMs and one stator with discontinuous HTS was studied and created. However, simulations and experimental tests showed that the rotor and stator with such design present discontinuities that causes asymmetries on the rotation and several stable and unstable angles, which prevents the SMB to rotate smoothly. In order to eliminate such unstable rotation, a continuous design of the stator and/or rotor is required.

Due the very high cost of superconductor materials, the solution found was to replace the discontinuous rings of PMs used previously by three NdFeB radially magnetized ring PMs with grade N40 (Br=1.25 T). These magnets are pretended to have similar features, when compared with the previously layout of the PMs. However, due to manufacturing limitations, there are some differences. The outer diameter is 79 mm instead of 83 mm, whilst the inner diameter is 55 mm instead of 59 mm. The main concern was to keep the thickness (12 mm). The width remains 25 mm as well. The weight of the three rings together is 14.715 N. In Fig. 2.1 the magnetization type, dimensions and a real example of the ring PM are shown.

2.1.1 Design

Fig. 2.2 and 2.3 show the design and disposition of the the HTSs and new rings based PMs for the new SMB.

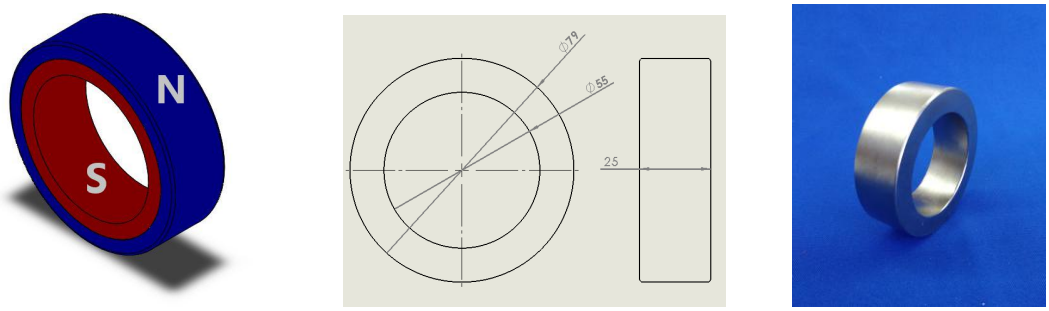

(a) Magnetization type (radial) (b) Ring PM dimensions (c) Ring PM

Figure 2.1: Ring Permanent Magnet.

The three ring PMs are magnetized in alternate North-South-North way. The distance between each ring defines the type of rotor and it is important, since levitation and guidance forces vary with it. Thus, three different rotors are studied: D5, D10 and D20, that have 5, 10 and 20 mm, respectively, between each PM. The detailed geometry and dimensions of the new SMB design are shown in Fig. 2.2 and 2.3, where rotor D5 and D20 are represented, respectively. The polarization configuration is shown in Fig. 2.4

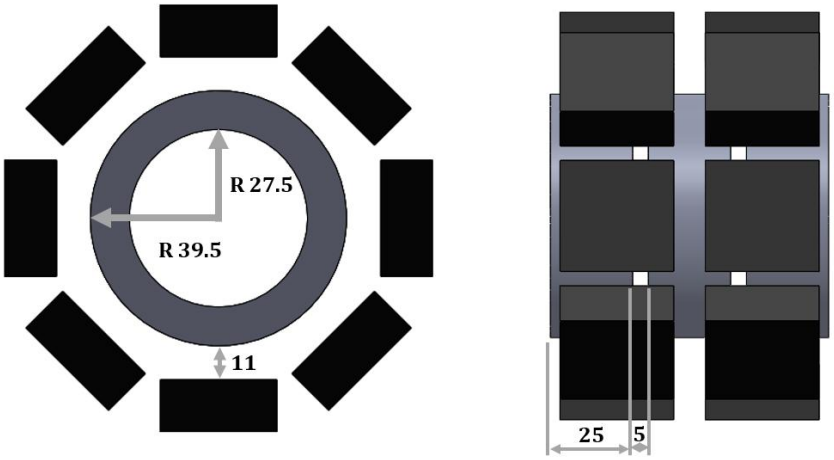

Figure 2.2: Detailed geometry and dimensions of the new SMB design - rotor D5.

2.1.2 Simulation

Based on the design shown above, a model was created to predict the involved magnetic forces of the system, in order to understand if such design is stable. To find a stable state of levitation, the levitation forces must support the weight of the ring PMs, besides the guidance forces must be enough to keep the rotor inside the stator.

In [19] a model based on the linear HTS magnetic levitation system using a ZFC technique is used to create the frictionless rotating bearing model with cylindrical geometry. Based on this study the Maxwell stress tensor, T_n, i.e., a tensor used in classical electromagnetism to represent the interaction between electromagnetic forces and mechanical momentum, is given by $T_n = -\frac{\mu}{2}|B_t|^2$, where B_t is the magnetic flux density tangential component and μ the magnetic permeability. This model also considers

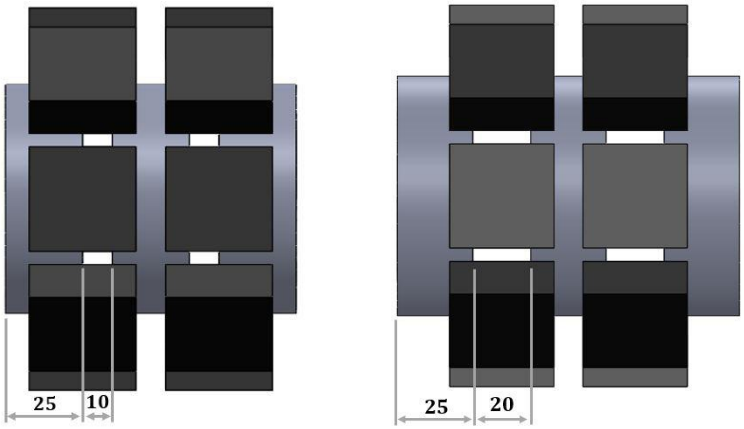

(a) D10 (b) D20

Figure 2.3: Detailed geometry and dimensions of the new SMB design - rotor D10 and D20.

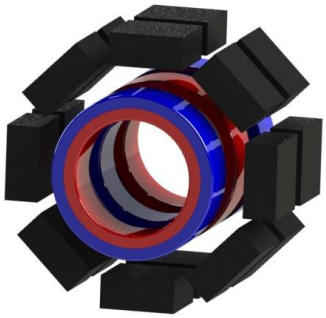

Figure 2.4: Magnetic poles distribution.

the relative permeability, μ_r of 0.2 on the superconductor walls. Hence, simulations have been done to predict the magnetic flux density involved in the system (Rotor+Stator with 6 HTS) for different Rotors (D5, D10 and D20) with the system stopped, i.e, with absence of rotation, and with the rotor centered radially and axially. In Fig. 2.6 and Fig. 2.7 [33] are represented the magnetic flux density involved in the ring PMs SMB for transversal and longitudinal view, respectively. D10 is not represented, since it has intermediate values.

Fig. 2.5 shows the directions of the Guidance and Levitation forces.

By analysing Fig. 2.6 and Fig. 2.7, it is expected that D5 has the highest Levitation Force, because the flux density is higher between the rotor and stator area, whereas D20 the highest Guidance Force, because the flux density is higher between each ring PM.

From this point, it is possible to calculate the forces involved between PMs and HTSs. Based on the same model [19], Levitation Forces, F_S, are calculated by $|F_S| = \frac{A}{\mu}\frac{|B_t|^2}{2}$, where A is the surface parallel to the xy plan.

In Fig. 2.8 the Levitation Forces between the 3 different rotors for different vertical eccentricities are compared. Gravitational forces are not considered. Eccentricity to be zero means that the rotor

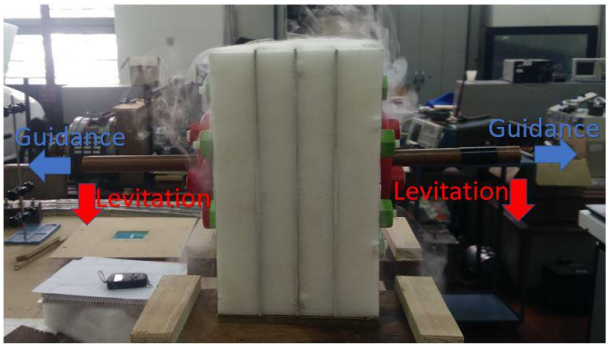

Figure 2.5: Levitation and Guidance forces direction.

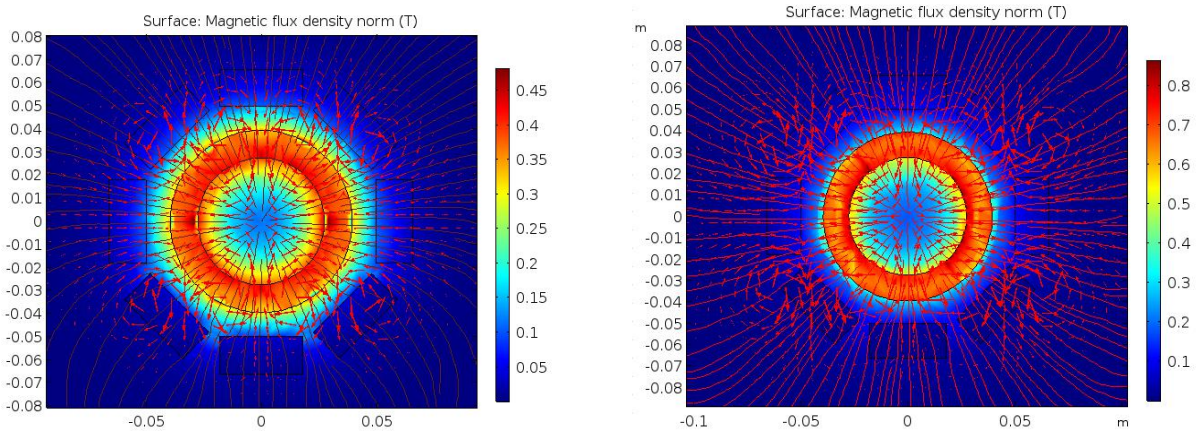

(a) D5 (b) D20

Figure 2.6: Magnetic flux densities prediction - transversal view [33].

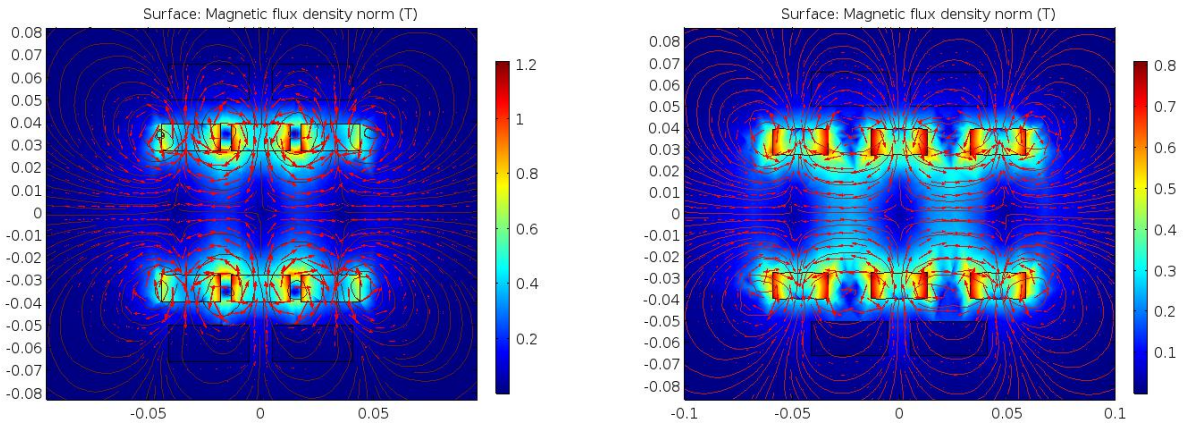

(a) D5 (b) D20

Figure 2.7: Magnetic flux densities prediction - longitudinal view [33].

is centered, i.e., the rotor and the stator are concentric. Positive values of eccentricity mean upward displacements, whilst negative values mean downward displacements.

In Fig. 2.9 is compared the Guidance Forces between the 3 different rotors for lateral misalignments . The initial position (Misalignment = 0 mm) corresponds to the point, whose rotor is balanced in the stable position centered inside the rotor.

Fig. 2.8 and Fig. 2.9 prove that any of the three rotors is able to sustain the total weight of the

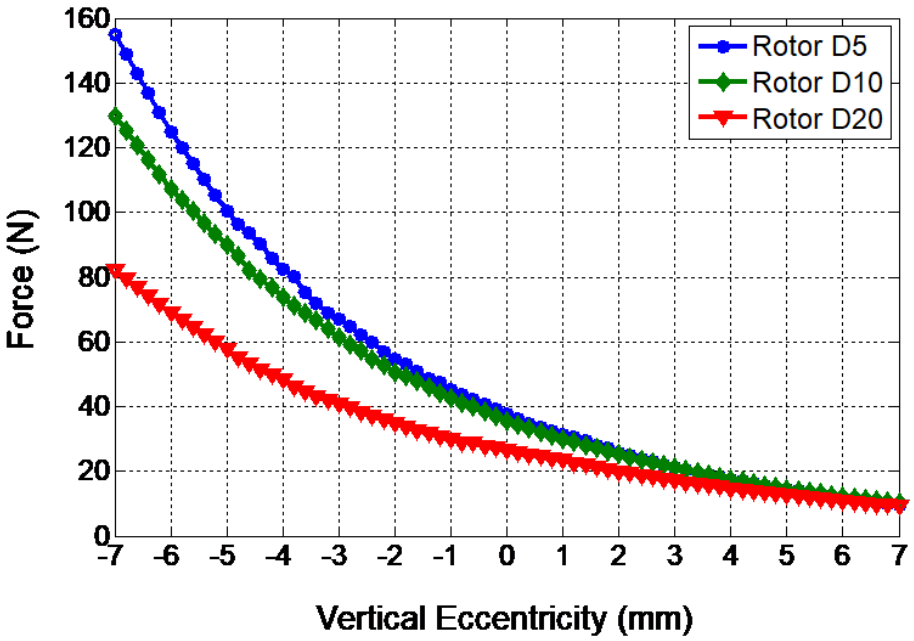

Figure 2.8: Levitation rotor forces for different values of vertical eccentricities. Results for the three different rotors are presented.

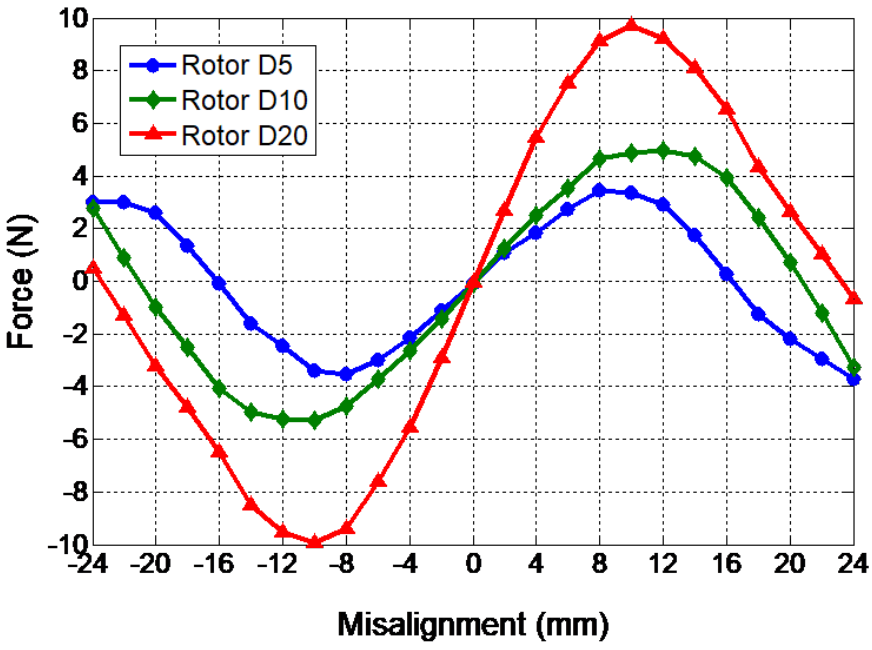

Figure 2.9: Guidance rotor forces for different rotor lateral misalignment values. Results for the three different rotors are presented.

PMs, thus indicating that the rings based SMB is viable and self-sustainable for both horizontal and vertical rotor eccentricity values. Furthermore, guidance forces increase as the distance between the

PMs increases, whereas the sustaining forces decrease, as briefly presented in Table 2.1.

Table 2.1: Levitation and Guidance forces for different rotor dimensions.

Rotor type	Levitation forces for centered rotor	Maximum Guidance forces
D5	36.9 N	3.5 N
D10	34.8 N	5.3 N
D20	26.5 N	9.7 N

These results show that adapting the geometry of the SMB is possible to fulfil different requirements, namely to increase the levitation forces or guidance stiffness.

2.1.3 Conception

A 3D CAD software was used for the conception of the new rotor. In fact, this type of conception is quite simple and, since there are 3D printers available in our Institute, it is the most practical way to create. Furthermore, by adjusting the level of fulfilment of the printer, it is possible to obtain either lighter or stiffer structure, according to the requirements. In general, it is possible to create stiff structures with low weight.

The rotor must present circular geometry and it has to support the three ring PMs with the geometry presented in Fig. 2.2 and Fig. 2.3. Further requirements are:

1. to keep the distances between each ring PM and between HTSs and PMs (air-gap);
2. to allow an easy and practical assembly and disassembly, in such a way that the PMs' damage risks are as minimum as possible;
3. to be as light as possible, ensuring the stiffness of the structure;
4. to create a balanced structure, i.e. a symmetric structure in terms of weight;
5. to develop a modular prototype.

Four main parts were designed to fulfil the requirements of the structure: two internals slices to keep the pretended distances between each PM and two externals. One external slice and two internal slices hold the PMs in the required positions. A cap (external slice) closes the structure and balances the weight. Three threaded rods are used to maintain the structure compact and six M10 nuts are used to assemble both stator and rotor together.

Single components: Fig. 2.10 shows the internal slice with a mounted PM. Fig. 2.11 and Fig. 2.12 show the external slices. A threaded rod and a nut used to assemble the structure are shown in Fig. 2.13 and Fig. 2.14, respectively.

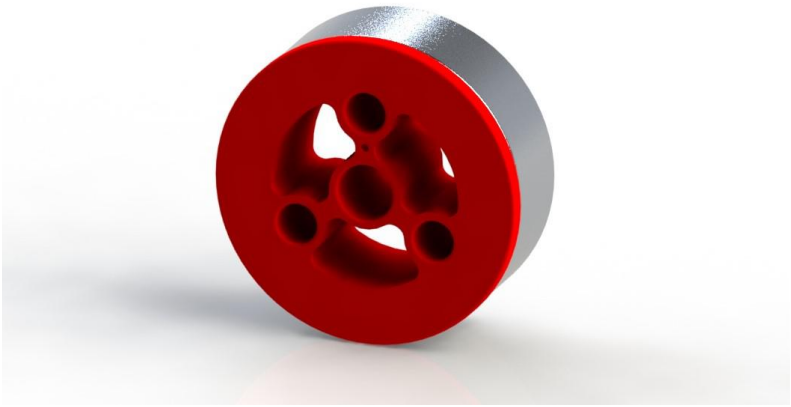

Figure 2.10: Internal slice with PM.

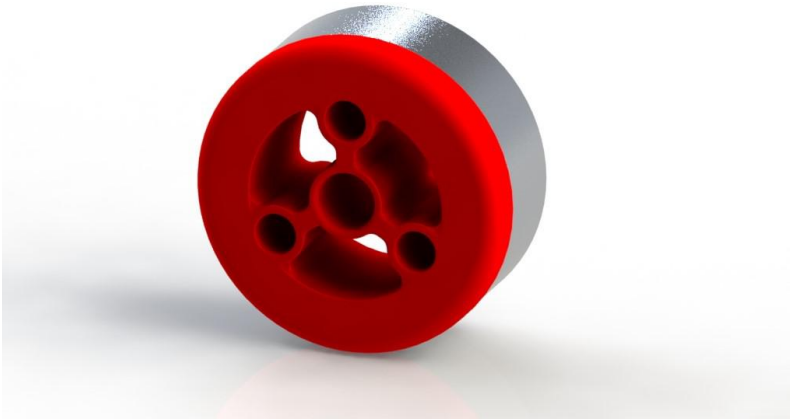

Figure 2.11: External slice with PM - base.

Figure 2.12: External slice with PM - cap.

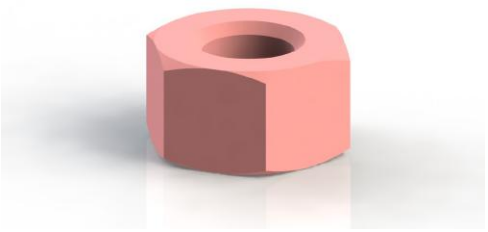

Figure 2.13: M10 Nut.

Figure 2.14: Threaded rod with a diameter of 10 mm and a length of 160 mm.

Assembly: The exploded view with the rotor D5 components is shown in Fig. 2.15. The final D5 rotor assembly is shown in Fig. 2.16 and the final SMB assembly in Fig. 2.17. The assembly technical drawings of rotors D5 and D20 are show in Fig. 2.18 and in Fig. 2.19.

Figure 2.15: Rotor exploded view.

Figure 2.16: Rotor assembly.

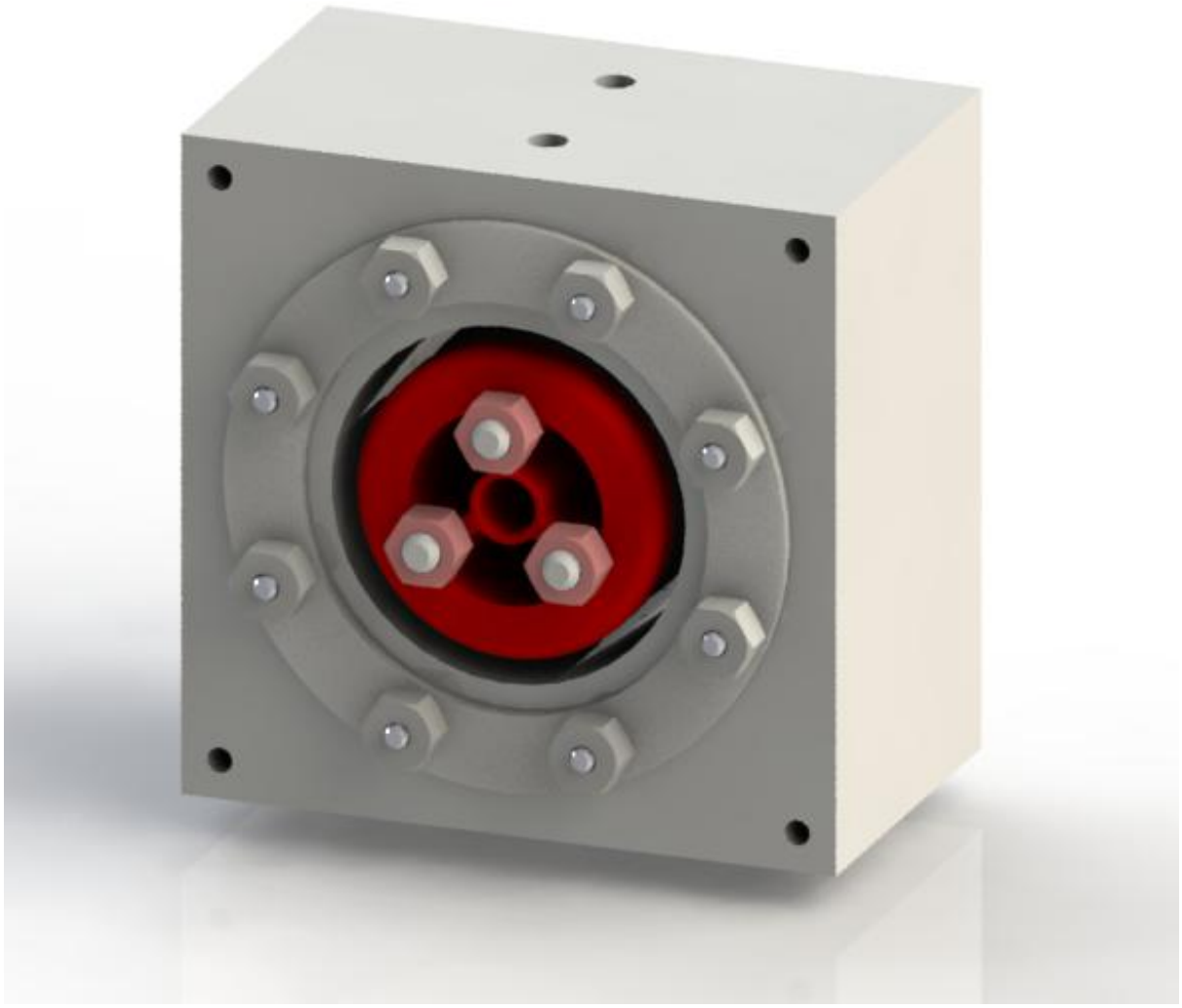

Figure 2.17: Final assembly.

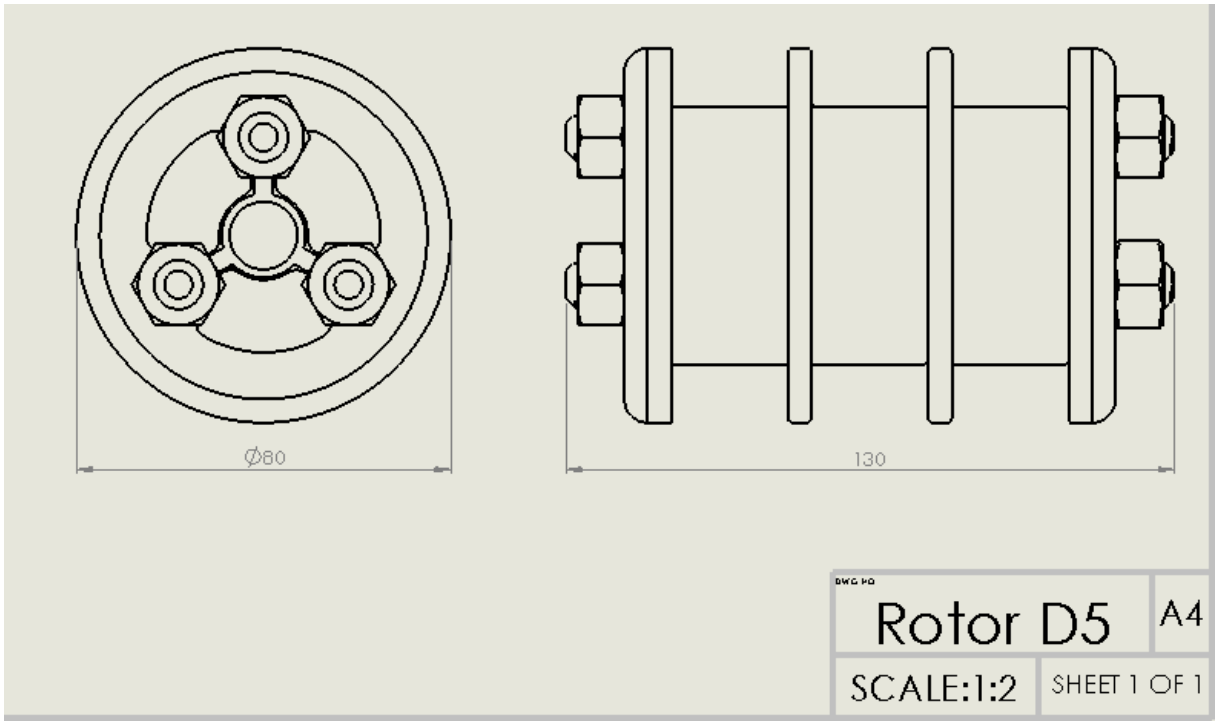

Figure 2.18: Technical drawing of the rotor D5.

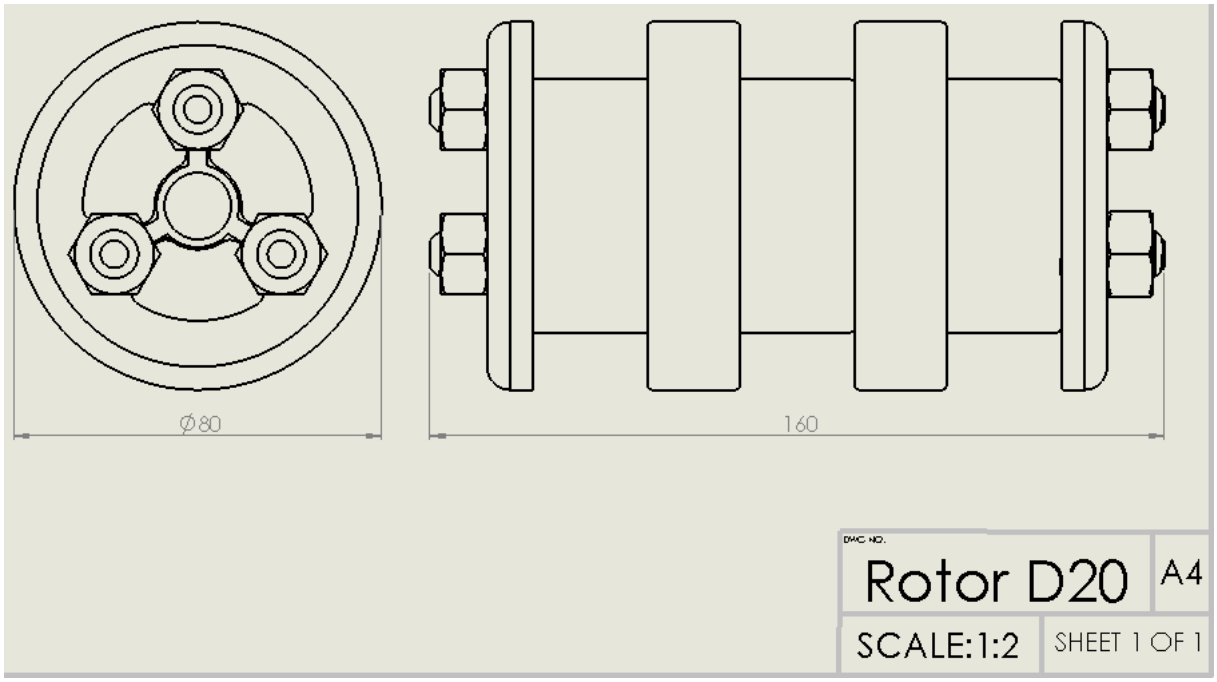

Figure 2.19: Technical drawing of the rotor D20.

2.2 Stator 2.0 - FEM Analyses and Conception

In this section, the analysis of the stator using a FEM software is made to evaluate how the structure may be developed to become thermally more efficient in terms of isolation.

2.2.1 Stator Heat Transfer Analysis

The thermal analysis of the component full of liquid nitrogen requires, besides the temperatures of the environment and the liquid nitrogen, the convection coefficient, h. To find this coefficient two different surfaces of the stator were considered. Fig. 2.20 shows the surfaces, whose h is considered as equal.

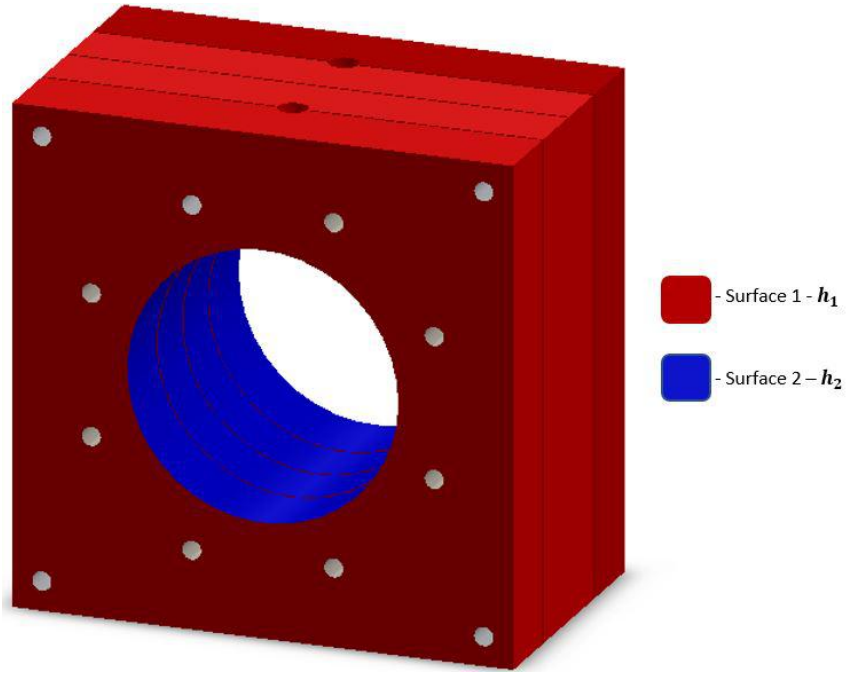

Figure 2.20: Surfaces with the same h.

To calculate h_1 and h_2, the surface temperatures T_s value are required. Thus, a thermometer CENTER 306, with measurement range from $-200\,°C$ to $1370\,°C$ and resolution of $0.1\,°C$, was used to measure the temperatures T_{s1} and T_{s2}, as shown in Fig. 2.21. As is possible to observe, $T_{s1} \approx 0\,°C = 273.15\,K$ and $T_{s2} \approx -90\,°C = 235.15\,K$. The room temperature was considered $T_\infty \approx 15\,°C = 288.15\,K$. Table 2.2 shows the thermophysical properties of air at the film Temperature, $T_f = \frac{T_s + T\infty}{2}$.

Table 2.2: Thermophysical Properties of Gases at Atmospheric Temperature [34]

Surface	**1**	**2**
T_f	$280\,K$	$235\,K$
Heat conductance, k	$24.7 \times 10^{-3}\,W/(m\,K)$	$21.2 \times 10^{-3}\,W/(m\,K)$
Kinematic viscosity, υ	$14.11 \times 10^{-6}\,m^2/s$	$10.25 \times 10^{-6}\,m^2/s$
Prandtl number, Pr	0.717	0.725
Thermal diffusivity, α	$19.7 \times 10^{-6}\,m^2/s$	$14.2 \times 10^{-6}\,m^2/s$
Expansion coefficient, β	$3.6 \times 10^{-3}/K$	$4.3 \times 10^{-3}/K$

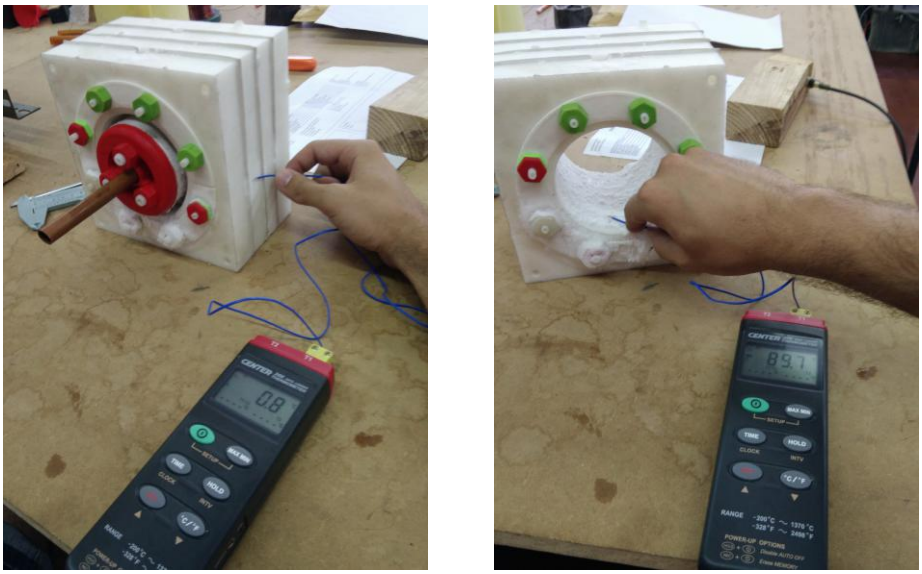

Figure 2.21: Temperature measurement in two different surfaces.

In order to calculate h_1 and h_2, surface 1 is going to be approximated to a Vertical Plate with height, L, of 0.170 m and surface 2 as a Long Horizontal Cylinder with diameter, D, of 0.092 m, as explained in [34] for exercises of free convection. Hence, the Rayleigh numbers, Ra, are given by

$$Ra_L = \frac{g\beta_1(T_{s1} - T_\infty)L^3}{\alpha_1 \upsilon_1} = 9.36 \times 10^6 \tag{2.1}$$

$$Ra_D = \frac{g\beta_2(T_{s2} - T_\infty)D^3}{\alpha_2 \upsilon_2} = 1.16 \times 10^7 \tag{2.2}$$

where g is the gravitational acceleration. Both results show that $Ra < 10^9$, hence there is no transition to turbulent regime. The Nusselt number, $\overline{Nu}$ can be then calculated by

$$\overline{Nu}_L = 0.68 + \frac{0.67Ra_L^{1/4}}{[1 + (0.492/Pr_1)^{9/16}]^{4/9}} = 29.15 \tag{2.3}$$

$$\overline{Nu}_D = [0.6 + \frac{0.387Ra_D^{1/6}}{[1 + (0.492/Pr_2)^{9/16}]^{8/27}}]^2 = 29.84 \tag{2.4}$$

Finally, it is possible to obtain the values of convection coefficient using

$$h_1 = \frac{\overline{Nu}_L \cdot k_1}{L} = 4.24\,\mathrm{W/(m^2\,K)} \tag{2.5}$$

$$h_2 = \frac{\overline{Nu}_D \cdot k_2}{D} = 6.87\,\mathrm{W/(m^2\,K)} \tag{2.6}$$

Using a FEM software, a model was created to thermally analyse the stator. Fig. 2.22 shows the chosen mesh of 10.3 mm per element used in the simulations.

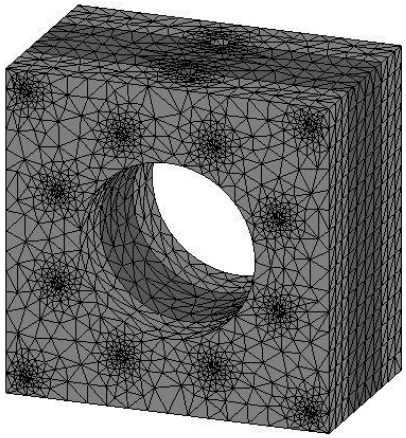

Figure 2.22: 10.3 mm mesh used in simulations.

Hence, the convection coefficients h_1 and h_2, besides the room temperature T_∞, were applied to the external surfaces. To the internal surfaces of the stator was applied an internal temperature, $T_i = 77\,\text{K}$, in order to simulate the contact with the liquid nitrogen.

Fig. 2.23 and Fig. 2.24 show the simulated temperature of the stator in steady-state. The temperature values achieved are lower than the measured in the experiments. This may be explained by the simplifications in calculation of the convection coefficients.

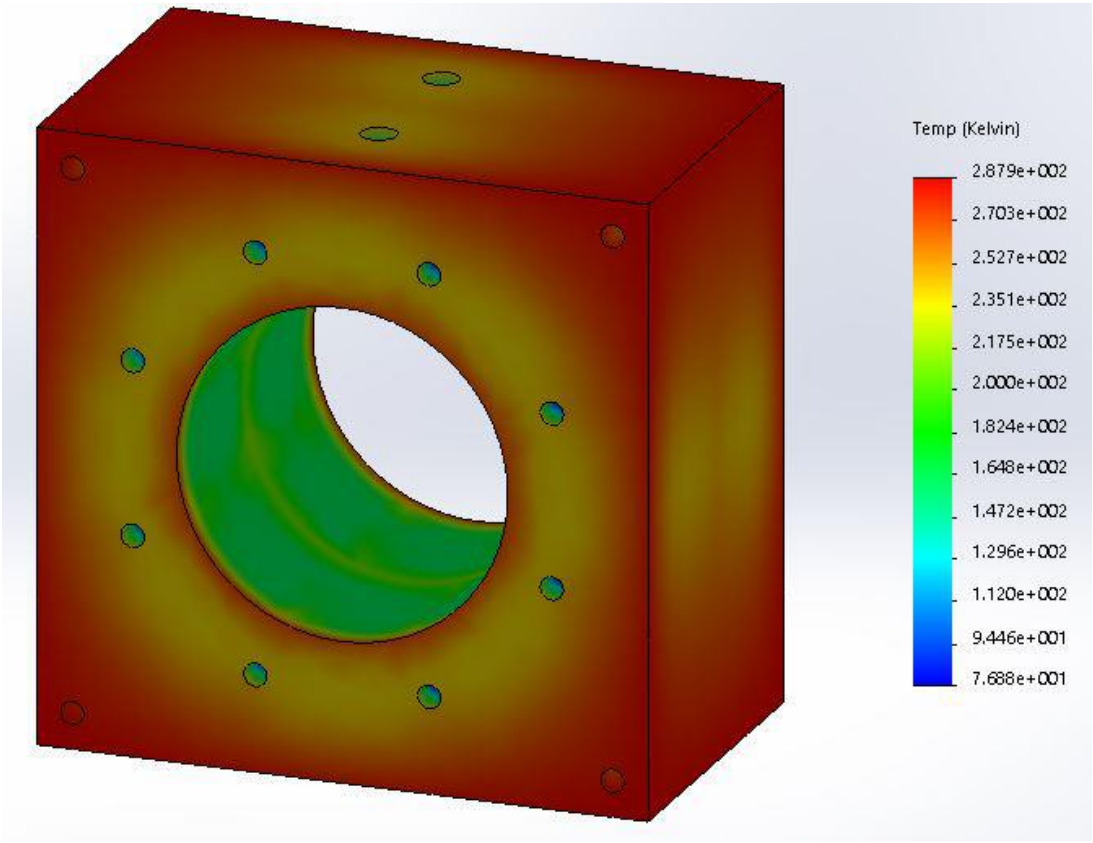

Figure 2.23: Simulated external temperature.

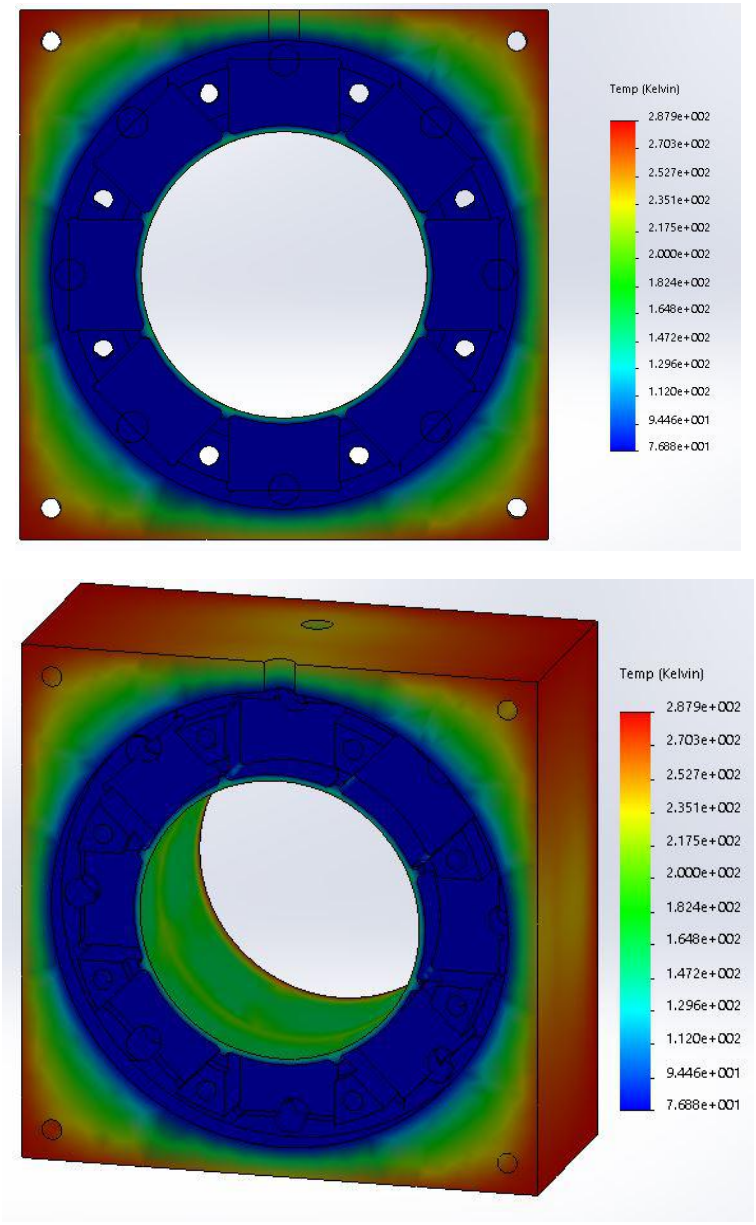

Figure 2.24: Simulated internal temperature.

Based on the FEM simulation, the rate of heat transfer is 37.445 W. The input energy required to change the state from liquid to vapour at constant temperature is called the latent heat of vaporization. The liquid nitrogen latent heat of vaporization , h_e, is 199 kJ/kg at atmospheric pressure [34]. The evaporation rate of the liquid nitrogen is calculated by

$$\frac{\delta m}{\delta t} = \frac{q}{h_e} = \frac{37.445}{199.10^3} = 0.000\,188\,\mathrm{kg/s} = 11.29\,\mathrm{g/\,min} \tag{2.7}$$

which is 14.4% (error percentage) higher than the values measured by the experiments. In fact, the value of liquid nitrogen vaporization rate measured in [1, 32] was 9.67 g/min. The error may be related with the two upper holes used to refill the stator, that were not considered in the simulations and/or by the simplifications used throughout the exercise.

2.2.2 Thermal Isolation Analysis

In order to improve the stator structure in terms of thermal isolation, a new hypothesis is going to be evaluated on this subsection. Notice that, by analysing the model developed in subsection 2.2.3, the lowest external temperature was obtained in surface 2 (Fig. 2.20). Hence, it is also this surface which presents the highest heat flux, since it also presents the highest thermal gradient. Moreover, the referred section wall has 2 mm of width and throughout the experiments developed in [20] and in this thesis, it was the local where the stator more frequently cracked, due to thermal fatigue.

Therefore, a stator with a thickness of 4 mm in walls of surface 2 was modelled and analysed thermally, in order to realize if the improvements are significant in terms of thermal isolation and liquid nitrogen evaporation rate reduction. The same convection coefficient, $h_2 = 6.87\,\mathrm{W/(m^2\,K)}$ was used as simplification. Moreover, all conditions of the analysis done in the previous subsection 2.2.3 remained the same.

The results of the energy transferred with thickness of 2 mm in surface 2 (subsection 2.2.3) and with 4 mm are presented in Fig. 2.25 and Fig. 2.26, respectively.

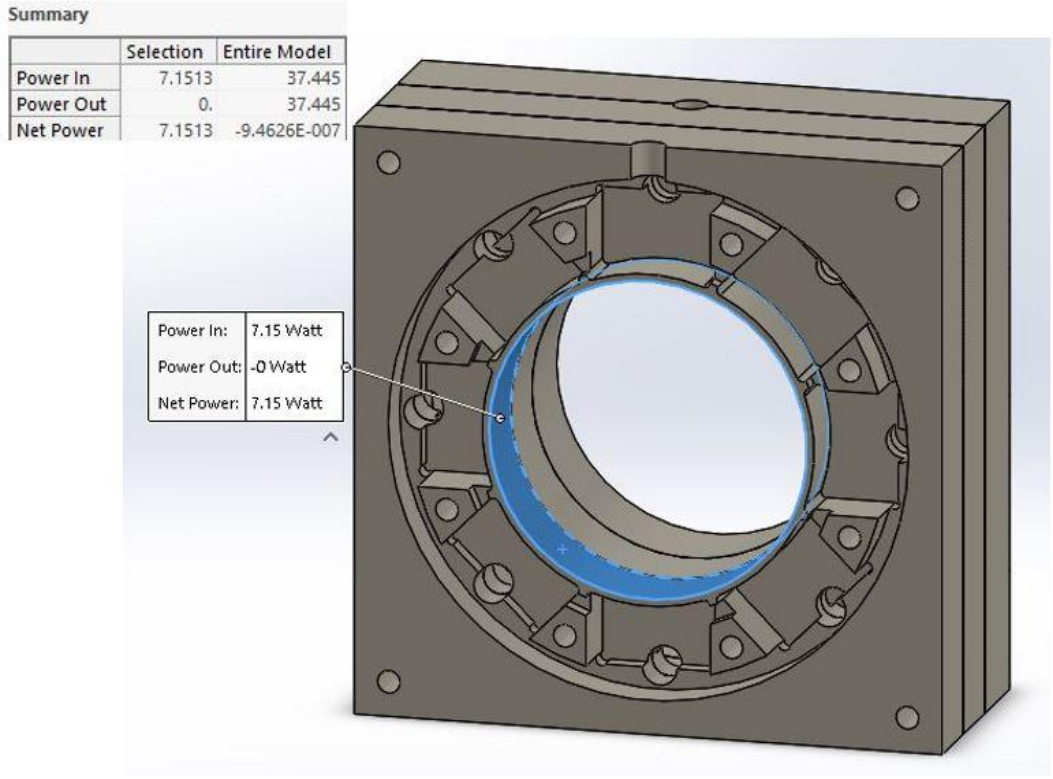

Figure 2.25: Total stator heat flux with surface 2 with 2 mm of thickness.

Analysing the result, it is possible to conclude that the heat flux rates of the selected section represented in blue (Fig. 2.25 and Fig. 2.26) and the whole system decrease from 7.15 W to 5.28 W and from 37.445 W to 31.445 W, respectively. According to the simulation, the liquid nitrogen evaporation rate, calculated as in section 2.2.1, would decrease from 11.29 g/min to 9.45 g/min in the simulated values, which corresponds to a decrease of 16.3 %,. Thus, a noticeable improvement in the isolation of the structure would be achieved with the new configuration.

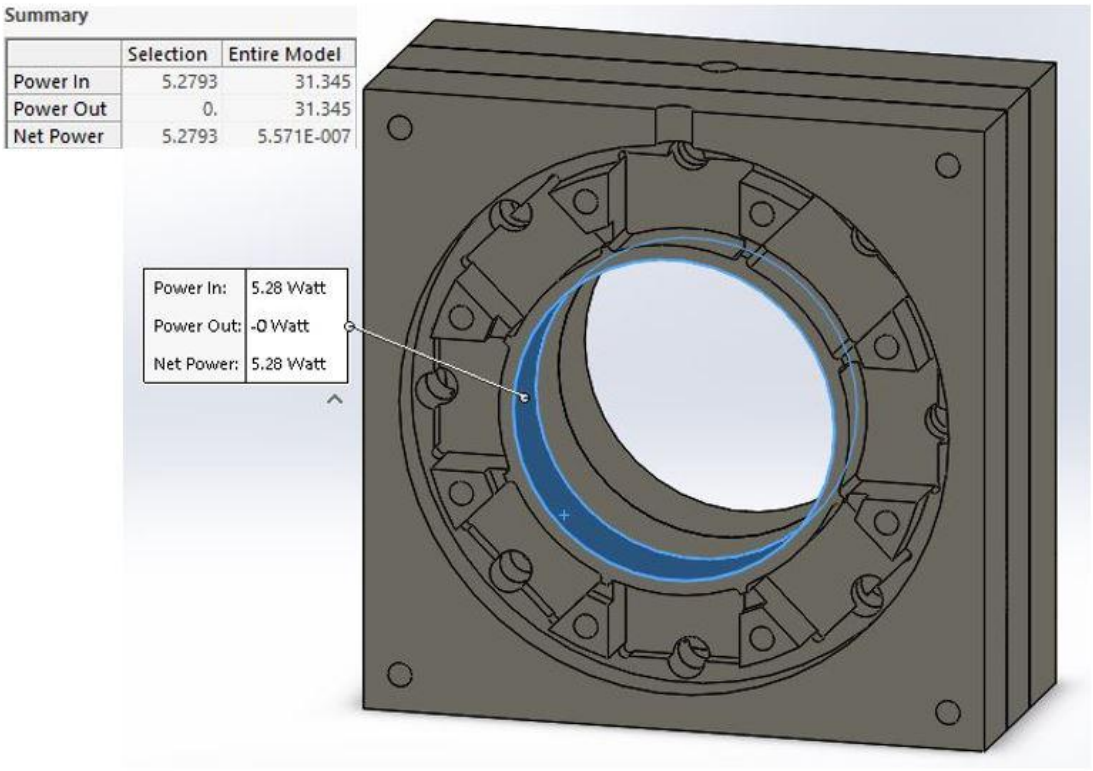

Figure 2.26: Total stator heat transferred flux with surface 2 with 4 mm of thickness.

Fig. 2.27 and 2.27 show the predicted temperature values with the new stator configuration.

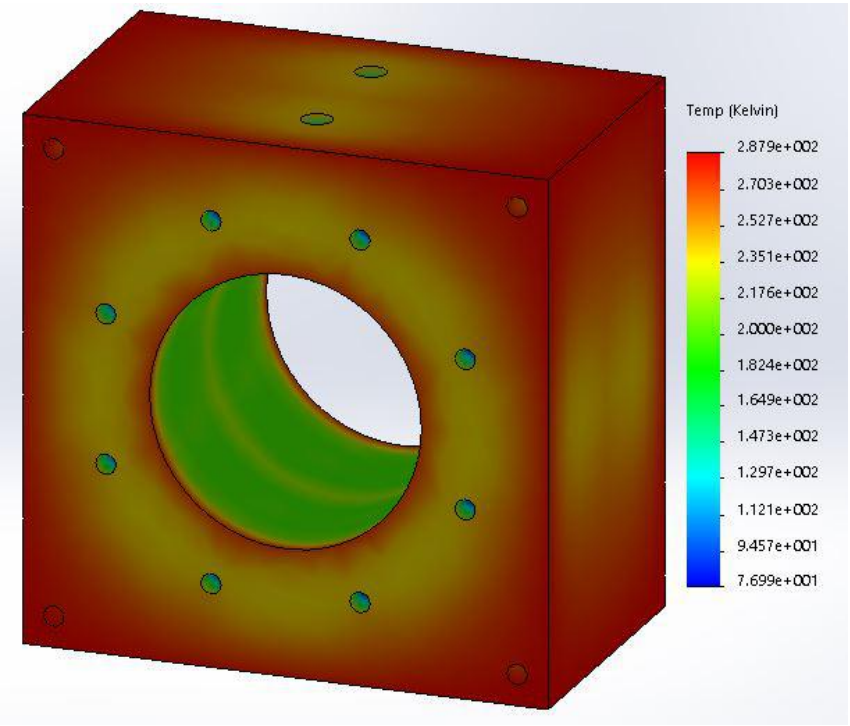

Figure 2.27: Simulated external temperature with the new stator configuration.

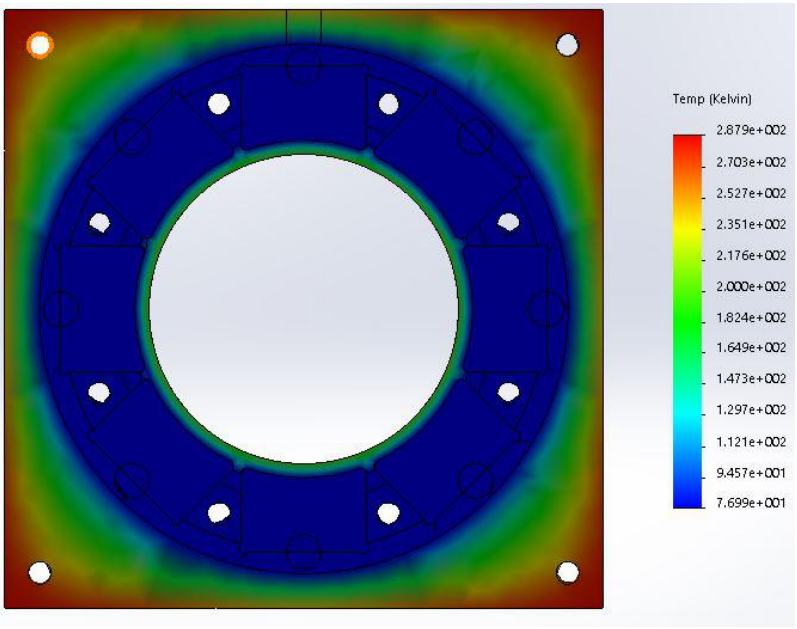

Figure 2.28: Simulated internal temperature with the new stator configuration.

2.2.3 Conception

As analysed in the previous subsections, a considerable improvement of the SMB stator thermal isolation may be achieved increasing the thickness of a stator wall of section 2. Moreover, the same wall revealed the most of the crack appearances throughout the experiments due to thermal fatigue. An example of a crack is shown in Fig. 2.29.

Figure 2.29: Crack observed in the referred wall.

Such cracks must be avoided, since they increase the liquid nitrogen consumption. Increasing the stator wall from 2 mm to 4 mm, could decrease the Nitrogen consumption and crack appearances. The technical drawing for the new rotor configuration is presented in Fig. 2.30. The change observed is present in the wall thickness. For a question of simplicity, a unique internal slice is represented.

Notice that the new configuration would only be practicable for the new ring PMs rotor, since it has lower diameter.

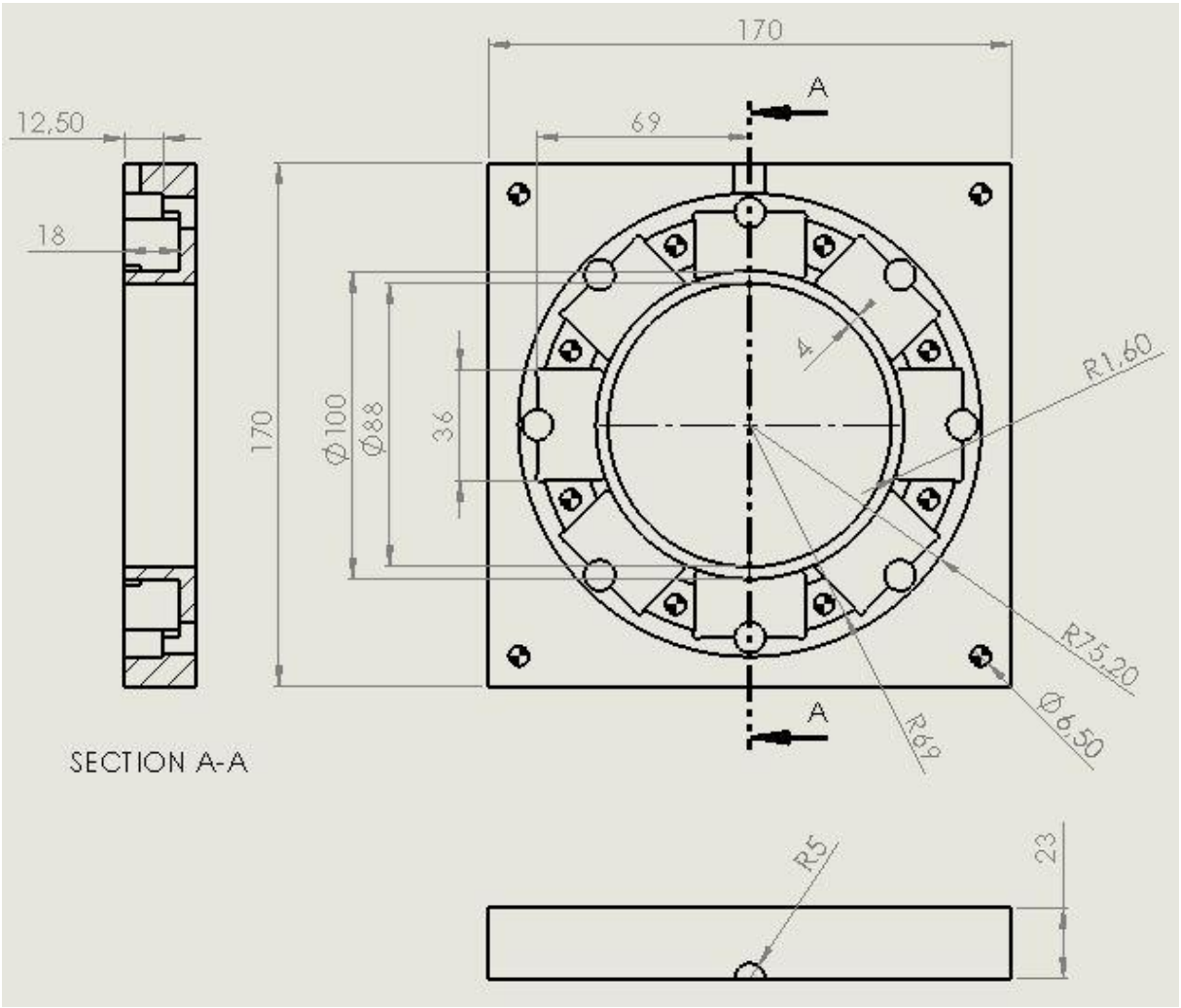

Figure 2.30: Internal slice of stator new configuration.

2.3 SMB as Bearing for Electrical Machines - Setup Conception

Previous works have analyzed features and forces involved, but only static tests were performed. Dynamic tests are required to realize if the frictionless bearing is able to support rotation. In fact, after analysing levitation and guidance forces measured before, it is possible to predict that the SMB is able to operate as a real bearing.

In this section, a setup is going to be created to evaluate the SMB behavior operating as a real bearing. The main objective is to replace a mechanical bearing from a electrical machine, in order to understand if the SMB sustains the weight of the system and rotates in a stable way. The bulks based PM rotor D5 was used in this section for all strategies and calculations.

The setup must include an electrical motor and the SMB, besides a shaft to link both components. Further requirements are:

1. to remove a mechanical bearing from the motor, in order to replace it;
2. to ensure that the motor operates in the previous conditions;
3. to create a safety structure, avoiding damage in the SMB and the electrical motor;
4. to find longitudinally the ideal distance between the SMBand the motor, in order to have an equilibrium between the SMB levitation forces and the weight of the system;
5. to control the motor speed, in order to test the SMB in different speed conditions.

Fig. 2.31 shows the first proposal of the setup. The conceived components to fulfil the requirements are identified and presented in Table 2.3.

Table 2.3: Outline Components .

Number	Designation	Function
1	SMB (discont. PM rotor D5)	-
2	Eletric Motor	-
3	Wooden Board	To support and fix all the components
4	-	To avoid the movement of the SMB (longitudinal)
5	Protector	To protect the stator from possible oscillations and/or misalignments
6	Shaft axial holder	To avoid the motor's rotor to come out from the stator
7	Supports	To elevate the motor to align it with the SMB

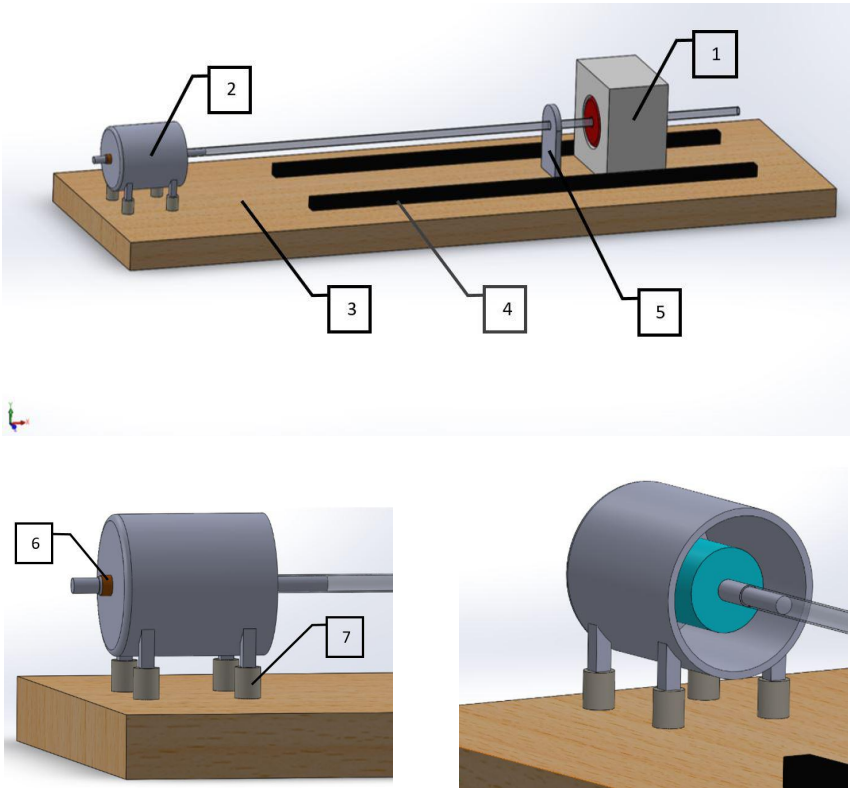

Figure 2.31: Outline projected.

The electric motor of Fig. 2.32 was given in for such purpose. It is a single-phase induction machine with synchronous speed of 2845 rpm at 50 Hz with 1.3 A . The air-gap between the rotor and stator is about 0.5 mm and the rotor has a diameter of 55.5 mm. An one meter shaft was used to make the connection between the motor and the SMB.

Figure 2.32: Single-phase induction motor

Since the electrical motor air-gap is 0.5 mm and oscillations are expected, a large distance would be recommended to avoid short-circuit on the motor. However, considering probable misalignments or warps on the shaft, bigger the distance between the SMB and the motor, higher the oscillations on the rotor SMB, which may cause damages on the prototype. Hence, an equilibrium between these two aspects has to be considered.

On the other hand, knowing the levitation forces of the SMB, a static analysis may be done to ensure

the weight system is balanced with levitation forces, in such a way that the rotor is as centered inside the rotor as possible. In fact, considering that there are neither misalignments and warps nor oscillations, the best motor performance would be with the centered rotor. Fig. 2.33 shows the forces diagram used to the analyses, with forces vectors and distances from the point A, the point where the system is supported by the mechanical bearing.

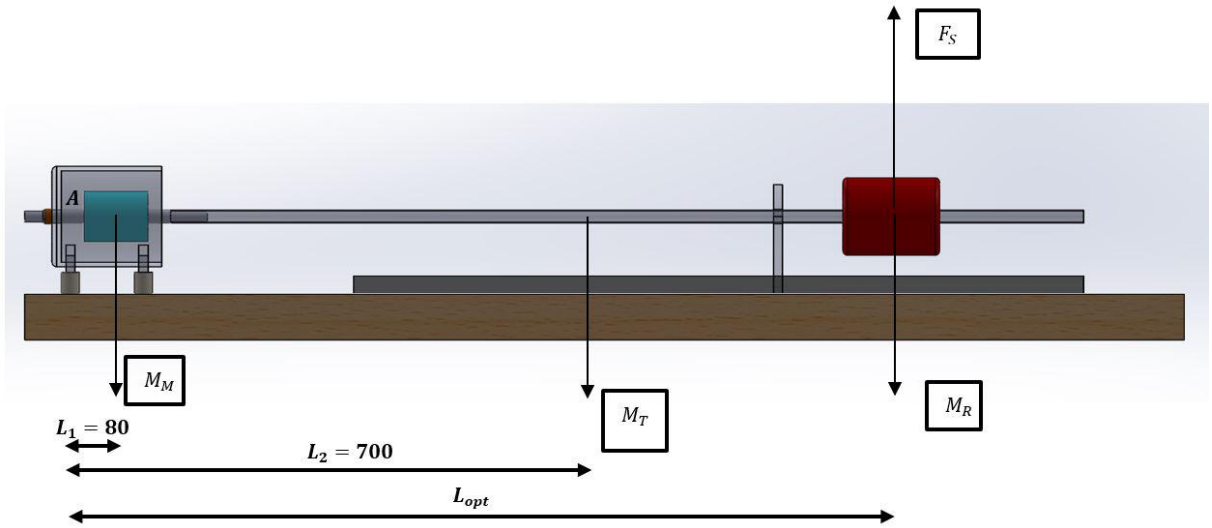

Figure 2.33: Force diagram of the system.

Table 2.4 and Table 2.5 describe the forces of Fig. 2.33 . The levitation forces of the Table 2.5 were obtained from previous experimental methods presented in [1].

Table 2.4: Involved forces.

Force	Designation	Intensity [N]
M_M	Motor weight	9.81
M_T	Tube weight	3.43
M_R	Rotor weight	10.18
F_S	Levitation forces	*See Table 2.5

Table 2.5: Levitation forces for different eccentricities [1].

Eccentricity [mm]	Measured Forces [kg]	Measured Forces [N]	Levitation Forces [N]
-1.75	2.096	20.5408	30.7132
-1.1	1.184	11.6032	2.7756
-1	1.076	10.5448	20.7172
-0.3	1.036	10.1528	20.3252
-0.25	0.898	8.8004	18.9728
0.4	0.724	7.0952	17.2676

To find the optimal distance the minimal eccentricity studied (-0.25 mm) was considered, in order to have the rotor centered. Thereby, the levitation force is 18.97 N.

Hence, the optimal distance is calculated by

$$\sum M_A = L_1 M_M + L_2 M_T + L_{opt}(M_R - F_S) = 0 \tag{2.8}$$

$$\Leftrightarrow L_1 M_M + L_2 M_T = L_{opt}(F_S - M_R) \tag{2.9}$$

$$\Leftrightarrow L_{opt} = 0.362\,\text{m} = 362\,\text{mm} \tag{2.10}$$

Fig. 2.34 shows the components projected and the whole system. There are some small differences, when compared with the first outline. However, the requirements are fulfilled.

(a) Protector

(b) Axial shaft holder

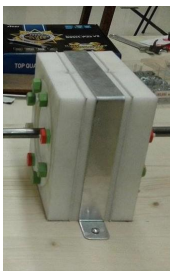

(c) Security Ribbon

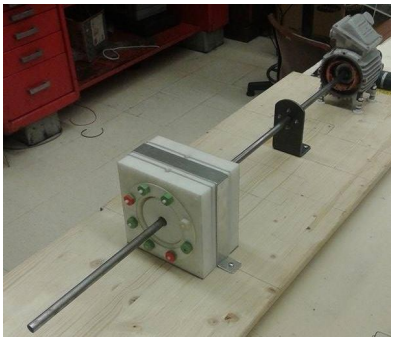

(d) System

Figure 2.34: Components and final assembly.

Furthermore, an Altivar 31 frequency inverter was set to allow soft starts of the motor and to control the angular speed of the motor. Fig. 2.35 shows the frequency inverter and the motor in star-connection.

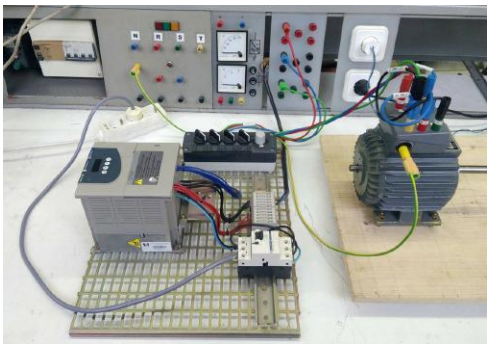

Figure 2.35: Frequency inverter used.

All the tests made using the setup in this section developed are present in section 3.2 and section 3.3.3.

Chapter 3

Experimental Part and Results

Experiments are the primary component of the scientific method. They are used to test theories and hypotheses about how physical processes work under particular conditions. In this Chapter, the motivations, methodology and results of the experimental part of the present work are described.

Firstly, the construction of the new rotors D5 and D20 based on the rings based PM rotor is described. Rotor D10 was not constructed, because the values of Levitation and Guidance forces for it are intermediate values. Afterwards, dry tests, i.e., tests without the usage of liquid nitrogen, hence in absence of superconductivity, are explained. These experiments have the main objective of ensure that there are conditions to use the setup described in section 2.3 to safety evaluate the SMB as a bearing for an electrical machine. Finally, tests with the usage of liquid nitrogen are going to be described, in order to evaluate important characteristics of the SMB developed during this work.

3.1 Rotor Construction

The chosen materials have relative magnetic permeability, μ_r, of about 1, which is verified in the most of the materials used in 3D printers. Thus, the rotor slices and the nuts are made of Polylactic Acid (PLA) in order to have high resistance and good finishing. They were built up using the *MakerBot Replicator* 3D printer, as shown in Fig. 3.1. A fill density of 30% was used in the print to save material and to make the final prototype lighter. The rods are made of Teflon (polytetrafluoroethylene) and were machined in a lathe machine.

The threads of the rods and nuts were made manually using a lathe machine. To save resources and time, the rods were conceived to be used in both rotors. Hence, the length of the rods is 160 mm (required length for D20), although the required length for the rotor D5 is 125 mm, as explained in Fig. 3.2. Moreover, each thread is 30 mm long (25 mm required + 2.5 mm tolerance).

Figure 3.1: 3D printer used to build the components printing rotor D20.

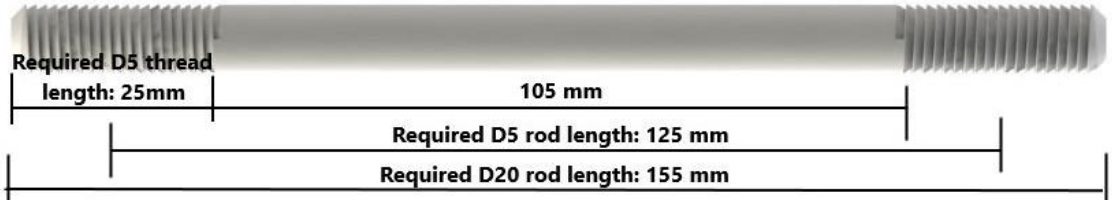

Figure 3.2: Required distances for the different rotors.

Next figures show the final product of the prototype conception and construction. Single components are shown, as well as the whole assembly dismounted and mounted. One rotor requires 4 slices, 3 threaded rods, 6 nuts and 3 ring PMs. Thus, Fig. 3.3 shows the single components that constitute the rotor D20, Fig. 3.4 shows the total set of the prototype D5 and Fig. 3.5 and Fig. 3.6 show the final prototype D5 and D20, respectively.

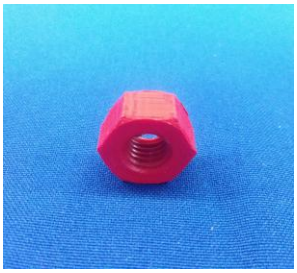

(a) Nut

(b) Rod

(c) External slice holding a PM

Figure 3.3: Single components of the prototype.

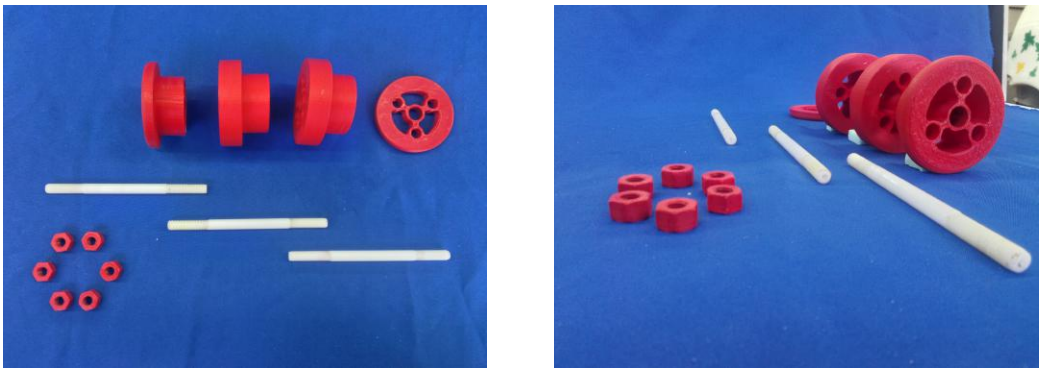

Figure 3.4: Rotor D20 assembly without ring PMs.

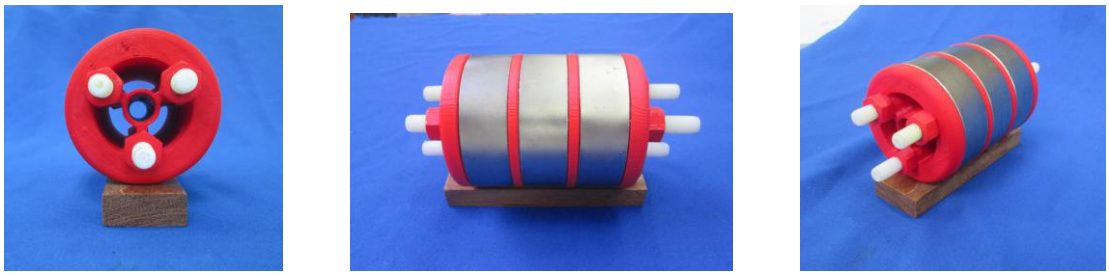

Figure 3.5: Final rotor prototype - D5.

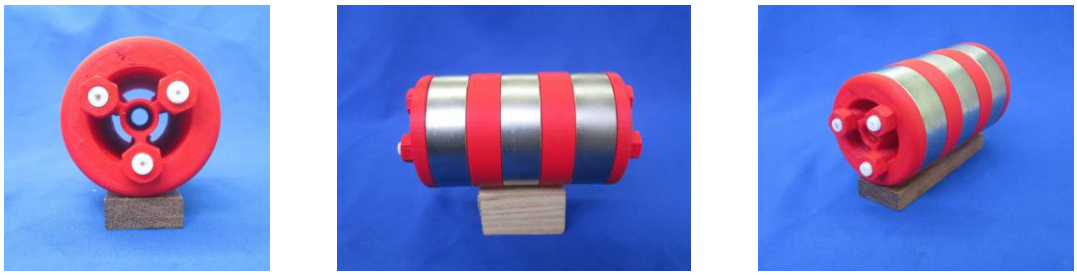

Figure 3.6: Final rotor prototype - D20.

The measured weight of the rotor D5 with PMs is 1.570 kg, while the rotor D20 is 1.620 kg.

Several tests were made to prove the stiffness of the structure and the easiness and security to mount and dismount the assembly.

3.2 Tests without Nitrogen

With all the components and the setup of section 2.3 created, the system was tested. Using the frequency inverter, the current was increasingly supplied to the motor. However, after several trials it was understandable that the electric machine would not work in such conditions, even with all components completely centered. The electromagnetic forces pull the rotor to the stator like a magnet, avoiding its rotation.

All the changes accomplished to solve the problem and to adapt successfully the setup are described in this section. Moreover, the installation of a fiberoptic sensor is described. With the use of this sensor, it is pretended to evaluate the behaviour and stability of the SMB operating as a bearing.

Notice that in the section, all experiments do not have usage of liquid nitrogen. The weight of the system is supported by the protector (Fig. 2.34 (a)).

3.2.1 Efforts to start the motor

As explained before, it was not possible to start the motor. After remove one of the mechanical bearing, the rotor does not rotate and it is blocked instead.

The first strategy to solve the problem was to create a new rotor with smaller diameter, in order to increase the air-gap and avoid the contact between stator and rotor. A rotor with 50 mm of diameter was created and it is shown in Fig. 3.7. Fig. 3.8 presents the dimensions and components of it.

(a) Original and new rotor

(b) New rotor inside the motor

Figure 3.7: Manufactured rotor for the electrical motor.

The shaft of the new motor's rotor is constituted by iron, in order to have good mechanical properties, namely stiffness. The rotor is made of aluminium, a light and paramagnetic metal. The use of aluminium was chosen to avoid the chance of the rotor to be attracted by the magnetic fields of the motor's stator, since aluminium is not a ferromagnetic material. Both components were manufactured in such a way the total weight was as minimum as possible.

After the previous modification, the rotor rotated, although the supply motor currents to overcome the stall torque were too high, which led to motor overheating. In fact, the currents involved to start the motor were around 4 A when the recommended limit to the motor is 1.4 A , which makes the experimental method unworkable.

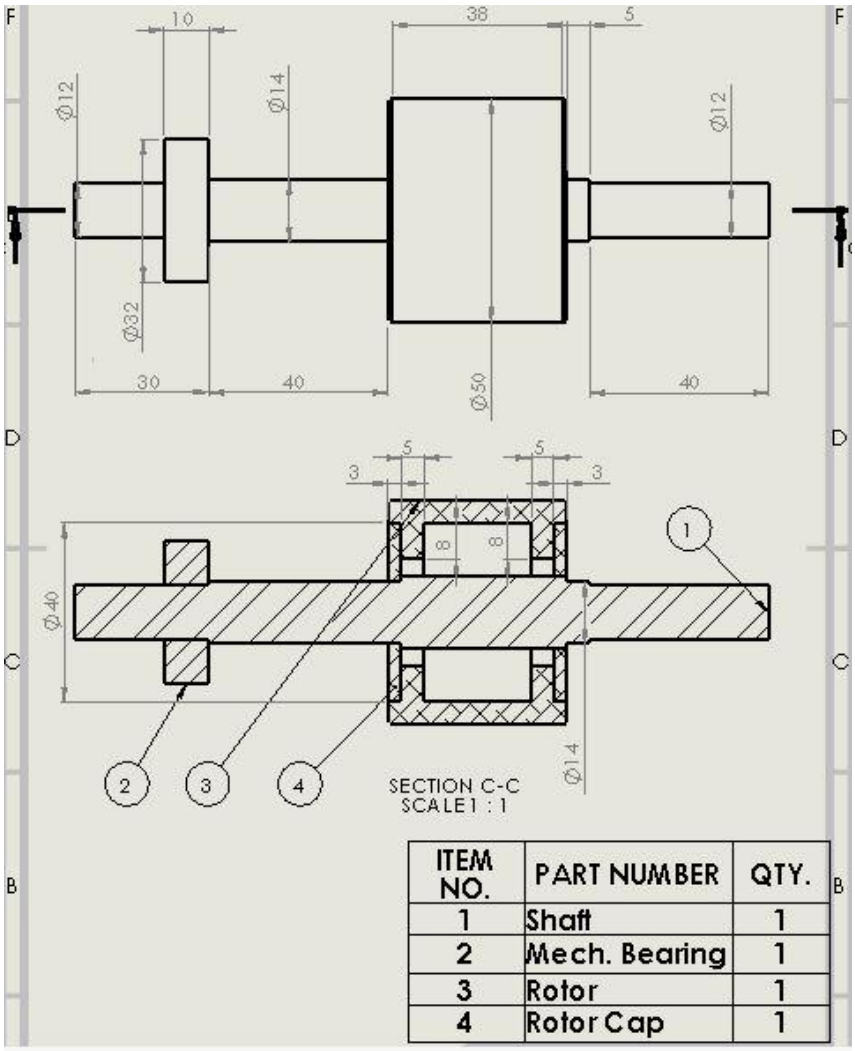

Figure 3.8: Manufactured rotor for the electrical motor technical drawing.

Trying to reduce the high current observed to start the motor, iron sheets have been placed inside the rotor as described in Fig. 3.9, in order to improve the magnetic flux conduction between rotor and stator, avoiding flux losses.

(a) Iron sheet

(b) Iron sheets placed inside the aluminiun rotor

Figure 3.9: Placement of the iron sheets.

The required supply current decreased to around 3 A, which is still far from the required 1.3 A.

A different approach was to reduce the resistive load, reducing the weight and, therefore, the current to start the motor. For such purpose, a can and a wood shaft were used to create a rotor as light as

possible. The iron sheets shown in Fig. 3.9 (a) were placed inside as well. The final product is shown in Fig. 3.10. Table 3.1 compares some properties between the original rotor and the ones created.

Figure 3.10: Rotor made from a can.

Table 3.1: Comparison between the available rotors.

Rotor	Diameter [mm]	Air-gap [mm]	Weight [g]	Supply current to start motor [A]
Original	55.5	0.5	≈ 1000	-
Aluminum	50	6	≈ 280	≈ 3
Can	55	1	≈ 80	≈ 3.5

Nevertheless, the currents involved were even higher, as it is possible to observe in Table 3.1.

The last and successful approach was to replace the single phase motor for a three-phase one with synchronous speed of 1370 rpm at 50 Hz with 1.13 A and it is presented in Fig. 3.11.

Figure 3.11: Three-phase induction motor.

The rotation starts with values around 1.5 A, which is still higher than the recommend limit, but that allows to carry out the experimental tests. Moreover, is it expected than, removing the friction through the usage of the SMB, the resistive load decreases.

A fan is used to ventilate the system (Fig. 3.12) and to avoid the overheating of the motor, which avoids permanent damage on it.

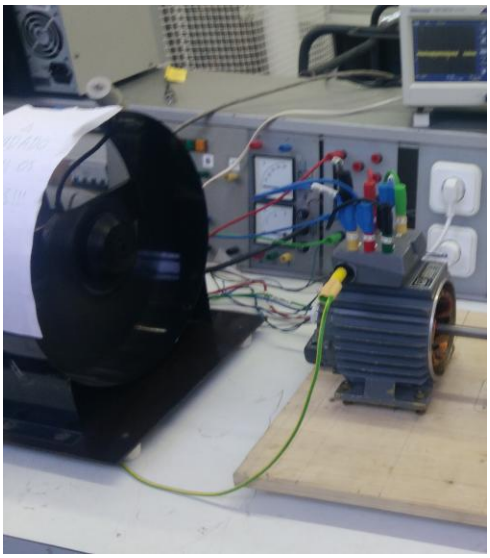

Figure 3.12: Motor's ventilation.

3.2.2 Fiberoptic displacement sensor

In order to evaluate the stability, oscillations and eccentricities of the system rotating, a displacement sensor with high accuracy is required, because the displacements may be smaller than a millimeter. The available sensor is a fiberoptic sensor PHILTEC, Inc. RC190 (Fig. 3.13).

Figure 3.13: Sensor PHILTEC, Inc. RC190.

The main specifications are present in Table 3.2. The sensor is supplied with 12 V and 0.12 A and the displacements are read in an oscillator. Notice that the sensor is able to measure displacement of micrometers and its linear range is 3.4 mm.

Table 3.2: Fiberoptic sensor PHILTEC, Inc . RC190 - Specifications.

Standard Specifications - RC190					
Light Source	LED, 850 nm	**Weight**	0.7 kg	**Total Range**	25.4 mm
Input Voltage	+12 V DC	**Tip Oper. Pressure**	15 bar	**Linear Range**	3.4 mm
Input Current	125 mA Max	**Tip Oper. Temperature**	-55 to 200 °C	**Nominal Standoff**	13.7 mm
Iso-thermal Drift	0.5 %	**Bandwidth**	3 dB down	**Nominal Sensitivity**	0.5 mV/μm
Oper. Temperature	0 to 70 °C	**Light Beam Spread**	25°	**Resolution**	7 μm

A supporter was created to hold the sensor in the required position to measure displacements of the shaft linked to the SMB. Sensor positions to measure horizontal and vertical displacement were considered. The supporter drawings and dimensions are present in the Fig. 3.14.

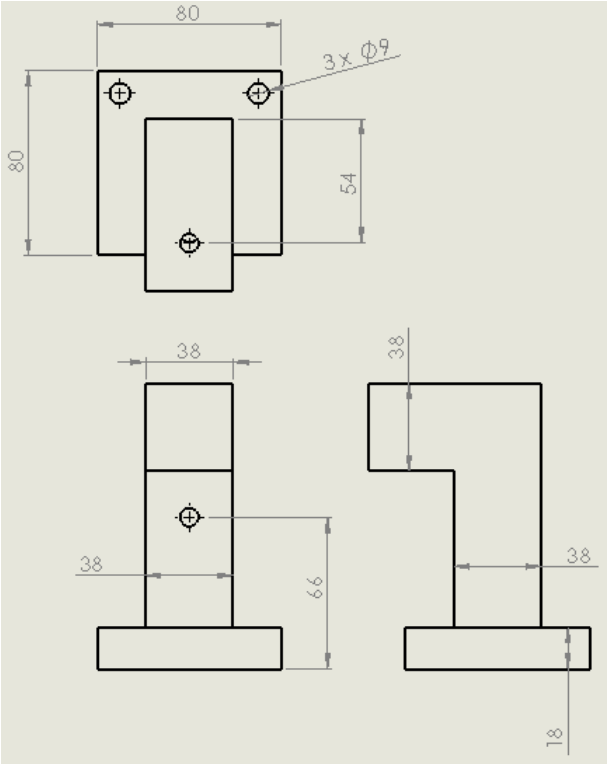

Figure 3.14: Sensor holder technical drawings.

After the construction of the supporter and sensor installation and calibration, the result is presented in the Fig. 3.15. Fig. 3.16 shows a successful test measuring the shaft displacement. The observable noise in the oscilloscope signal it is due to the usage of the frequency inverter. In fact, this device injects undesired harmonics in air and in electrical grid, which causes noise in the oscilloscope signal. Analysing signal frequencies instead of signal throughout time may be a solution to avoid noise perturbations.

(a) Sensor supporter

(b) Horizontal Measurement

(c) Vertical Measurement

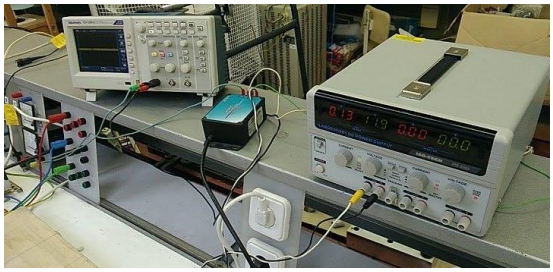

(d) Installation

Figure 3.15: Sensor's installation.

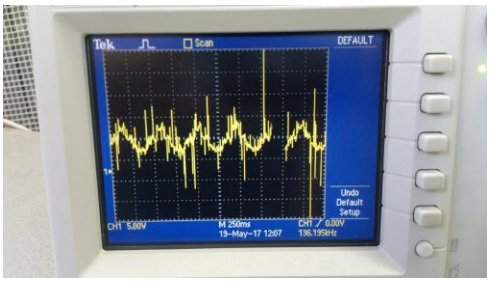

Figure 3.16: Sensor successful test.

Fig. 3.17 shows the final setup with all the components adjusted and the setup ready to test the SMB operating. The experiments accomplished using this setup are described in section 3.3.3.

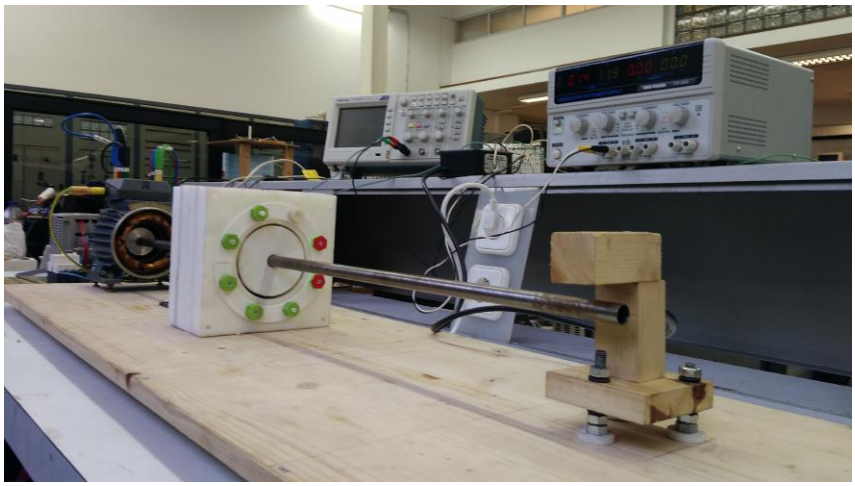

Figure 3.17: Final setup.

3.3 Tests with Nitrogen

As explained previously, the PMs and HTSs together allow to create very stable systems of levitation. This section describes the static and dynamic experiments accomplished using the superconducting levitation properties of the SMB.

Firstly, in order to validate the model used in section 2.1.2, a test is going to be done to measure Levitation and Guidance forces. Afterwards, dynamic tests are going to be performed, on one hand to analyse the behavior of the SMB operating as a bearing of an electrical machine and on the other hand to evaluate the dynamics of the present system. Furthermore, a experiment using the FC technique is used to test the viability of the SMB using this type of cooling.

3.3.1 Cooling Procedure

All the tests in section 3.3 (with exception of subsection 3.3.5) were made cooling the HTS in absence of magnetic field, i.e., following the ZFC technique. The same procedure used in [1] was followed. However, some extra steps were considered in order to increase the stator and HTSs time life.

The stator set without the rotor is firstly slowly inserted in a small Styrofoam box containing liquid nitrogen (Fig. 3.18), in order to cool the polyurethane of the stator at first, thus the superconductors surroundings. Only then, the liquid nitrogen is slowly poured to fill the stator up to the whole stator is completely full, achieving the ZFC superconducting state. The stator is then slowly removed from the Styrofoam box and the experiments can start. The liquid nitrogen is constantly poured to compensate the one evaporated.

(a) Stator inside the Styrofoam box containing liquid nitrogen

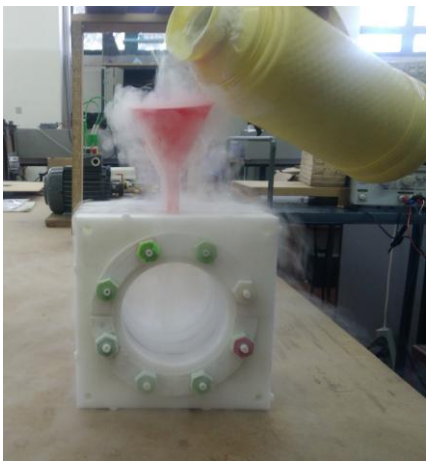

(b) Refiling the stator

Figure 3.18: Cooling the HTS.

After inserting the rotor inside the stator and using the new continuous rotor, the rotor does not touch any of the stator walls and remains balanced. It is quickly noticeable that the equilibrium is not obtained in specific angles anymore and the rotor reveals a smooth angular motion instead. Moreover, if an angular movement is induced, the rotor keeps its angular movement, working as a flywheel. Fig. 3.19 shows the rotor freely rotating.

Figure 3.19: Balanced rotor rotating in a free motion.

After each experiment, it is pretended the reheating of the stator to be smooth and slow, to avoid big thermal variations and, therefore, high thermal expansions. Thus, the stator set is dismounted after the evaporation of all liquid nitrogen. Fig. 3.20 shows the stator dismounted after an experiment with the HTS bulks still cold.

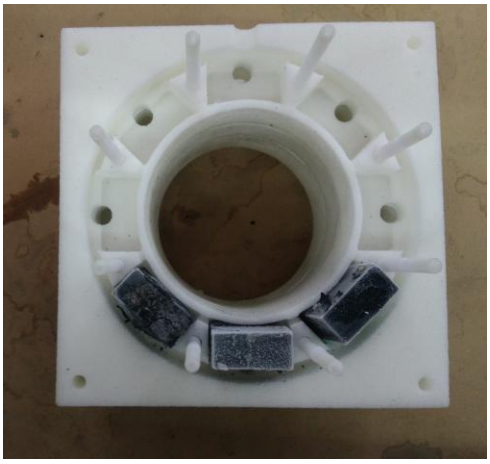

Figure 3.20: HTS cooled after an experiment.

3.3.2 Static Analysis

To measure levitation and guidance forces, similar setups and procedures were used to enable the comparison with the results obtained in [18]. The used method consists in measuring the forces in different positions of the rotor inserted inside the stator through a digital dynamometer (black device in Fig. 3.22 and Fig. 3.24). In order to force the displacement between stator and rotor, a screw with pitch of 0.8 mm is used to measure the distances. Levitation forces are measured in vertical direction, while Guidance forces in horizontal direction, as explained in Fig. 3.21. Tests using rotor D5 and D20 were performed to validate the results.

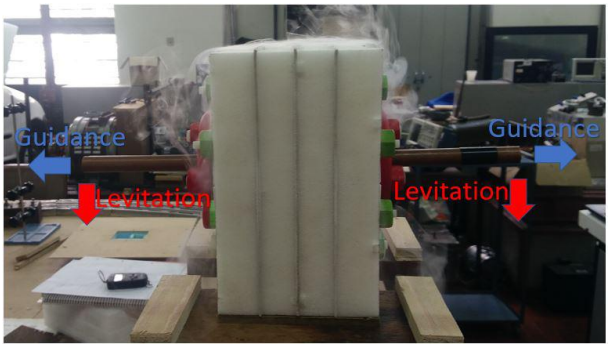

Figure 3.21: Levitation and Guidance forces direction.

Levitation forces

Fig. 3.22 shows the experimental setup used to measure Levitation forces. The rotor stays lifting, whilst the force is measured by the dynamometer. The rotor and the sensor are linked by a copper cable. This material was chosen, due to its high modulus of elasticity.

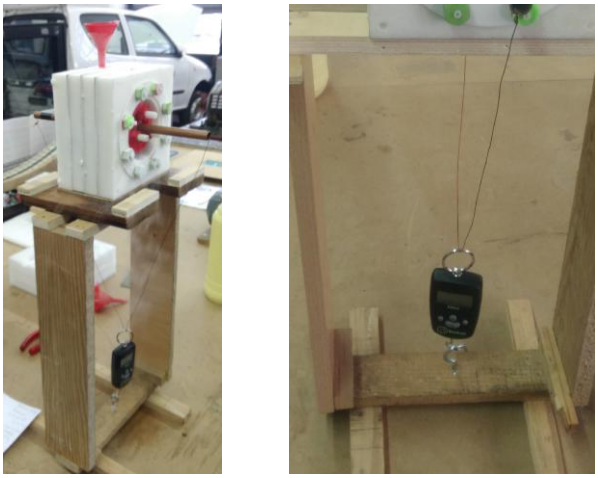

Figure 3.22: Experimental setup to measure lifting forces.

In Table 3.3 are presented the results of the experimental test for the levitation force measurement and Fig. 3.23 compares the values of forces obtained by experimental measurement with the ones by FEM simulation. Eccentricity to be zero means that rotor is centered in the middle of the stator. Positive eccentricities means eccentricities above the the center.

Table 3.3: Measured Levitation Forces for different rotor vertical eccentricities for rotor D5 and D20.

Eccentricity (mm)	-6.2	-5.4	-4.6	-3.8	-3.2	-3	-2.4	-2.2	-1.6	-1.4
D5 Meas. Force (N)	-	-	-	-	48.86	-	44.52	-	42.20	
D20 Meas. Force (N)	33.03	32.34	29.16	26.60	-	25.42	-	23.50	-	-21.70

Eccentricity (mm)	-0.8	-0.6	0	0.2	0.8	1	1.6	2.4	3.2	4
D5 Meas. Force (N)	33.73	-	30.26	-	26.89	-	24.40	21.27	18.76	17.34
D20 Meas. Force (N)	-	20.19	-	18.86	-	17.83	-	-	-	-

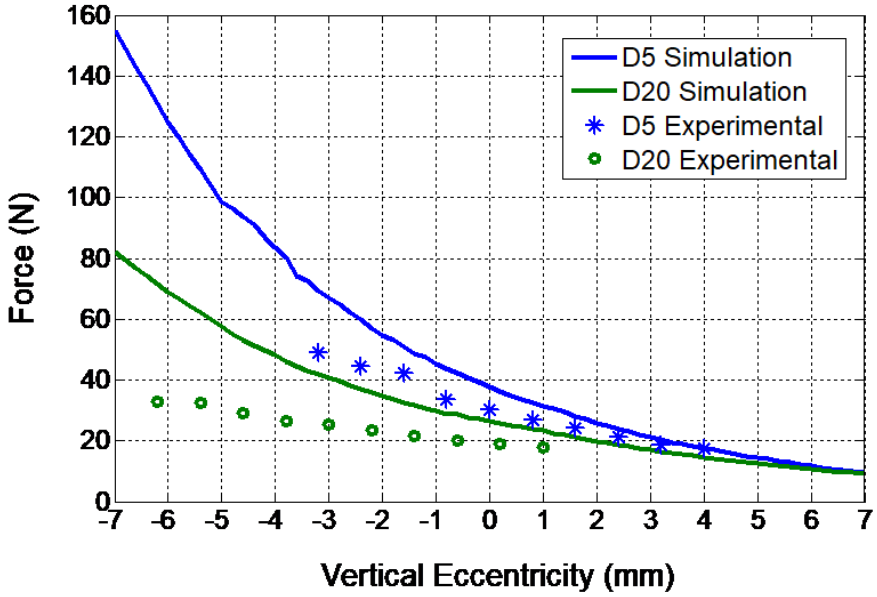

Figure 3.23: Rotor levitation forces versus vertical eccentricity for rotor D5 and D20.

The stable position for system, i.e., the position where the magnetic forces annul the weight of the rotor, is different for the two rotors, as expected. For the rotor D5 is 4 mm above the center, whilst for the rotor D20 is 1 mm. Moreover, levitation forces for rotor D5 are higher than for rotor D20. The measured levitation forces are lower than the estimated by the simulations. The difference is explained by simplifications used in the model of section 2.1.2. Furthermore, more negative are the values of eccentricity, higher the difference between simulated and measured values. Comparing with the results obtained in [20] with the discontinuous rotor, the levitation force is in general higher, which is compensated by the bigger weight of the rotor.

Guidance forces

Fig. 3.24 shows the experimental setup used to measure Guidance forces. The stator is laid upon a small car, whilst the rotor remains fixed centered in the stator. An axial stator misalignment is forced pulling the car in both directions, to measure the guidance forces that push or pull the rotor to its axial equilibrium position. Again, the screw is used to pull the sensor and, consequently, the stator, allowing a more precise measurement of the displacements.

In Table 3.4 are presented the results of the experimental test and Fig. 3.25 compares the values of guiding forces obtained by experimental measurement with the ones by FEM simulation.

The forces estimated show very good values, near to the simulated ones for rotor D5. For rotor D20 the guidance forces are slightly lower than predicted. However, the inflexion points are consistent. As expected, these forces are higher for rotor D20.

Figure 3.24: Experimental setup to measure guidance forces.

Table 3.4: Measured Guidance Forces for different rotor lateral displacements.

Displacement (mm)	-20	-18	-16	-14	-12	-10	-8	-6	-4	-2	0
D5 Meas. Force (N)	-	-	0	-1.29	-2.12	-2.53	-3.10	-2.59	-1.78	-0.33	0
D20 Meas. Force (N)	-3.2	-4.98	6.50	-8.5	-9.53	-9.95	-9.41	-7.63	-5.54	-2.89	-0.07

Displacement (mm)	2	4	6	8	10	12	14	16	18	20
D5 Meas. Force (N)	1.35	1.67	2.16	2.59	2.84	2.29	2.06	0	-	-
D20 Meas. Force (N)	2.70	5.47	7.52	9.147	9.72	9.21	8.10	6.51	4.35	2.65

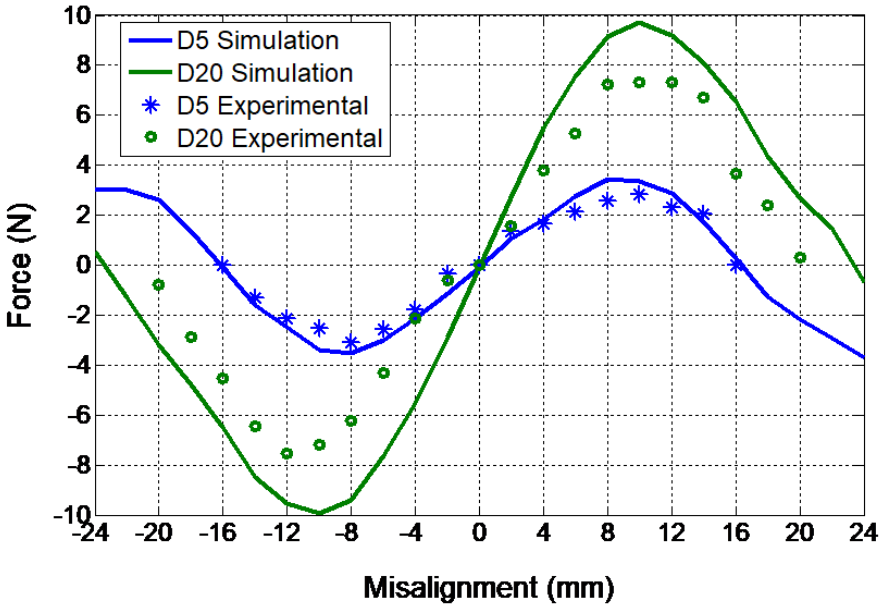

Figure 3.25: Rotor guidance forces versus vertical eccentricity for rotor D5 and D20.

Bulks based rotor forces vs. Rings based rotor forces

Table 3.5 compares the SMB force values using the old discontinuous rotor studied in [20] and the new continuous rotor based on ring PMs. The Fig. 3.26 shows the discontinuous rotor D5. Simulations and

experimental values of Levitation and Guidance forces are presented. In all the cases the force has increased using the new rotor.

Table 3.5: Sustaining and Guidance forces for discontinuous and continuous rotor.

	Sustaining Force for centered rotor		**Maximum Guidance Forces**	
Rotor type	D5 Simulation	D5 Experimental	D5 Simulation	D5 Experimental
Discontinuous Rotor	26.91 N	18.97 N (*)	3.12 N	2.16 N
Continuous Rotor	37.62 N	30.26 N	3.43 N	3.10 N
Difference	**139.8 %**	**159.5%**	**109.9%**	**143.5%**

(*)There are no data for null eccentricity in this case. The closest displacement of 0.25mm from the null eccentricity was used.

Thus, with the new design was possible to achieve higher forces with a lower diameter rotor and higher air gap distance, improving the operational security and equilibrium.

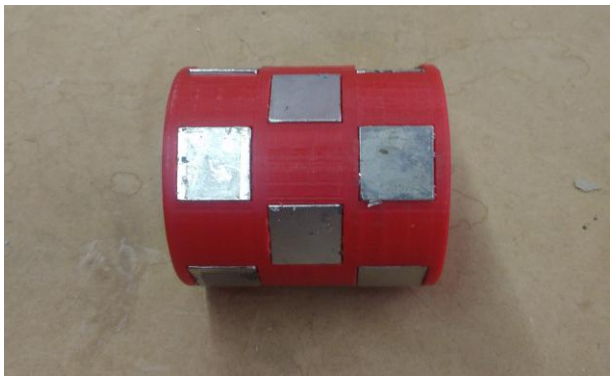

Figure 3.26: Discontinuous rotor D5.

3.3.3 Testing SMB as a Bearing for Electrical Machines

A big concern of our research team is to apply the SMB as a bearing for electrical machines. For such purpose, analyses are required to understand the viability of the SMB operating, i.e., to understand how the system behaves rotating. Thus, an experimental setup was prepared as referred in section 2.3 and section 3.2, on one hand to test the SMB as a bearing for electrical machines and on other hand to compare the stability and the smoothness between the operation of the SMB using discontinuous PMs [18, 19, 20] and the SMB using the new continuous PM rings.

The first concern was to test if the SMB was able to sustain the weight of the system and to rotate in a stable way at the same time. In the first experiments, the discontinuous rotor was used and, despite its small air-gap, they were successful. The system achieved speeds around 600 rpm. Furthermore, the system revealed quite stable at speeds above 300 rpm, which ensured the safety of the operation for the SMB. The system speed was measured through a digital tachometer RS 163-5348 (Fig. 3.28 (a)). Fig. 3.27 shows the setup of the first successful experiment.

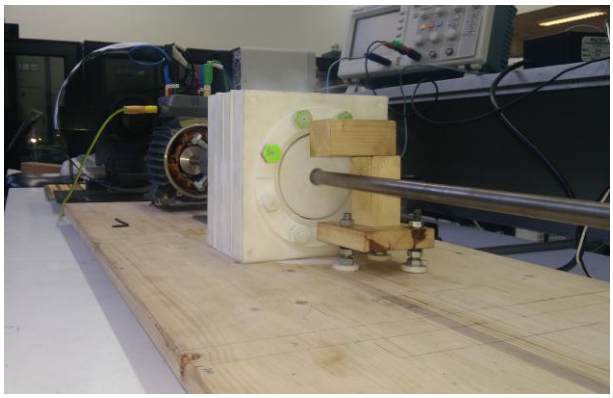

Figure 3.27: First successful test.

(a) Tachometer RS 163-5348 (b) Current Probe

Figure 3.28: Sensor used in the experiments.

To analyse stability, a current probe (Fig. 3.28 (b)) was set to evaluate the supply current and the fiberoptic displacement sensor was set to measure oscillations and eccentricities. The sensor is pointed to the shaft, as close as possible from the SMB.

Fig. 3.29 presents the experimental test using the continuous PM rotor D5.

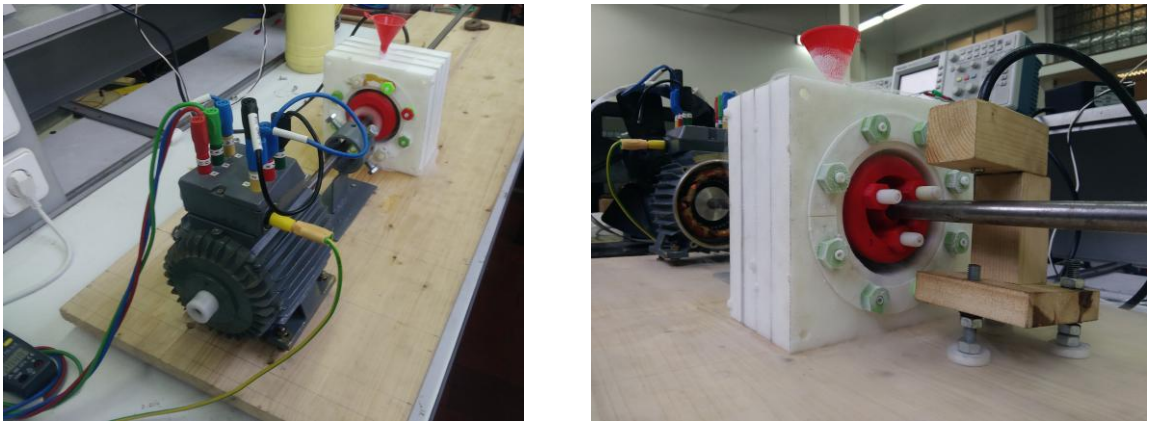

Figure 3.29: Experimental test of vibrations using continuous rotor.

Several tests with different angular speeds were made using the discontinuous PM rotor D5 and the continuous PM rotor D5. Results in time scale and in frequency scale were recorded. Hence, there are four different types of data to analyse: time and frequency measurements in supply current signal and displacement sensor. Fig. 3.30 shows the four kinds of data for an angular speed around 900 rpm with the continuous PM rotor.

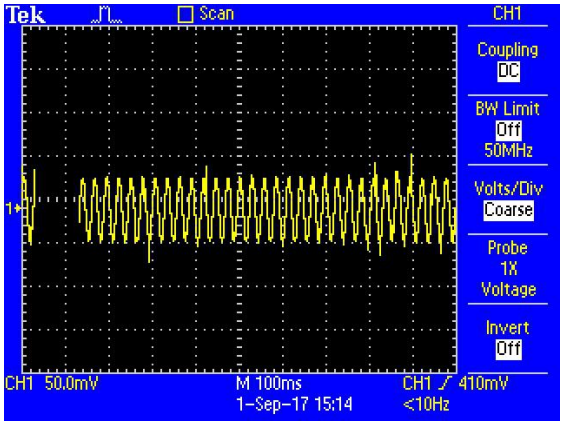

(a) Current signal througout time.

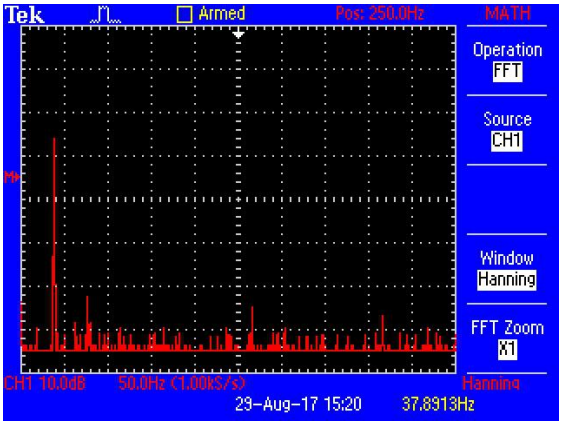

(b) Frequency current signal frequency.

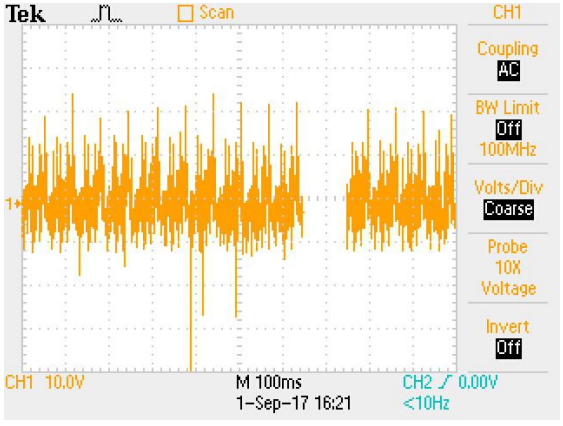

(c) Sensor signal througout time.

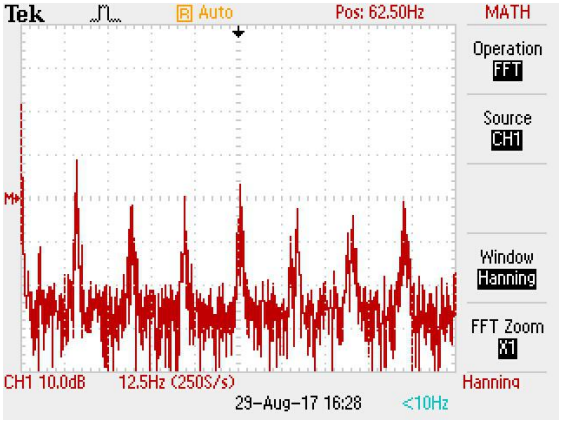

(d) Frequency sensor signal.

Figure 3.30: Recorded data using continuous rotor at 900 rpm.

Current signal fundamental frequency, i.e., the highest peak observed in Fig. 3.30 (b), indicates the value of frequency that comes from the frequency inverter and supply the motor. This value corresponds to the frequency of the observed sinusoidal signal in Fig. 3.30 (a).

The displacement sensor signal in time presents too much noise to analyse. In turn, the frequency signal has relevant information. Actually, the analyses of this kind of spectrum is a very useful and increasingly spread tool in problems analyses of electrical machines. In fact, FFT spectrum provide information to help in determination of sources and causes of problems and, with trending, how long until the problems becomes critical [35].

For all the tested rotor speeds, the spectrum of the signal from the displacement sensor consists in a series of frequency harmonics multiple of the fundamental frequency harmonic, f_s , that is approximately the same as the rotor angular frequency. This corresponds in time to a series of thin pulses with period $T_s = 1/f_s$. This kind of spectrum is generally associated with mechanical looseness in electrical motors [35] and it is observed when the bearings of the machine are not properly fixed, i.e., when there is free space between the bearing and the bearing support.

Fig. 3.31, Fig. 3.32 and Fig. 3.34 shows three displacement sensor FFTs with discontinuous and continuous PM rotor at speeds close to 500 rpm and with continuous rotor at 900 rpm to analyse the spectrum differences for different situations.

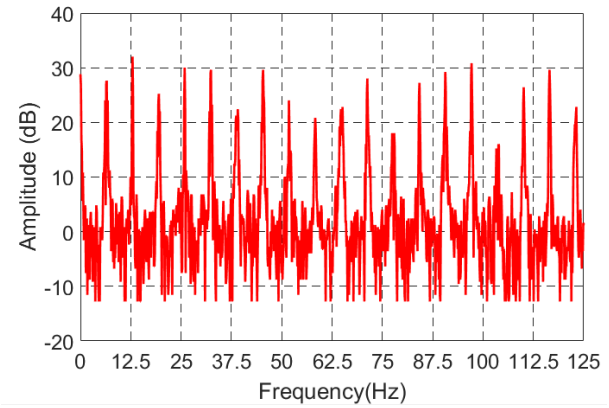

Figure 3.31: Displacement sensor spectrum, for discontinuous rotor at 550 rpm.

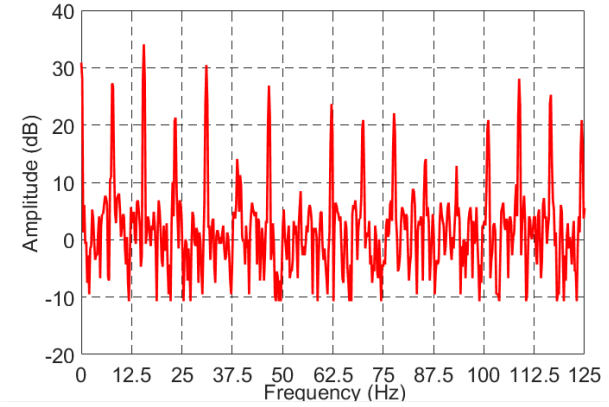

Figure 3.32: Displacement sensor spectrum, for continuous rotor at 500 rpm.

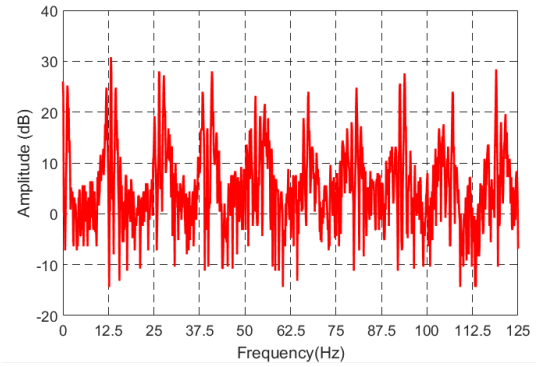

Figure 3.33: Displacement sensor spectrum, for discontinuous rotor at 900 rpm.

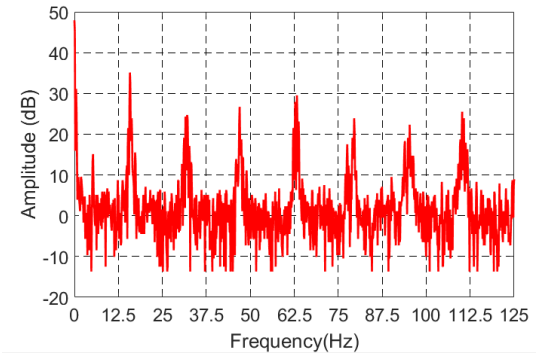

Figure 3.34: Displacement sensor spectrum, for continuous rotor at 820 rpm.

Table 3.6 shows the fundamental frequencies of the supplied current from the inverter and measured by the displacement sensor, for several rotor angular velocities tested. In this table, f_R is the rotor frequency of rotation measured by the tachometer, f_s the fundamental frequency of the signal from the displacement sensor and f_c the fundamental frequency of the supply current from the frequency inverter.

It is also show the operating slip s, calculated according to expression

$$s = \frac{f_c - p \cdot f_R}{f_c} \tag{3.1}$$

where $p = 2$ is the driving motor number of dipoles.

Table 3.6: Vibrations for several rotor speeds tested.

Rotor D5	$f_R(Hz) = \frac{rpm}{60}$	Sensor f_s (Hz)	Current f_c (Hz)	Slip s (%)
Discontinuous PM rotor	9.17 (550 rpm)	6.16	47	61
	13.2 (820 rpm)	11.96	50	47.2
Continuous PM rotor	4.17 (250 rpm)	4.39	17	50.9
	8.33 (500 rpm)	7.64	25	33.4
	15 (900 rpm)	14.61	40	25
	22.5 (1350 rpm)	22.93	50	10

It is pretended with Table 3.6 and Fig. 3.31 to Fig. 3.34:

1. to compare the behavior of SMB between Discontinuous and Continuous PM rotor. The strategy was to compare both rotors at the same angular speeds, however it was not possible to induce exactly the same speeds using the frequency inverter. Thus, the compared speeds are as close as possible. Furthermore, it was not possible to operate the discontinuous PM rotor closes to 250 rpm, because of the reduced air gap and the amplitude of vibrations. Also, it was not possible to operate the discontinuous PM rotor closes to 1350 rpm, because the maximal speed with this rotor was 820 rpm ($f_c = 50Hz$);
2. to analyse the behavior of both rotors for different speed values.

As explained before, f_R and f_s are approximately the same. They are not exactly equal due to inaccurate measurements with the tachometer. However, it is possible to conclude that the real speed of the system is given by $f_s \cdot 60$ rpm .

For rotor speeds close to 500 rpm, Fig. 3.31 and Fig. 3.32 show that the number and amplitude of harmonics from displacement rotor spectrum are generally higher for the discontinuous PM rotor. This suggests that the vibrations are higher for discontinuous PM rotor for speeds around 500 rpm. On the other hand, Fig. 3.33 and Fig. 3.34 show that for speeds close to 900 rpm the difference in the number of harmonics and their amplitude, observed between the discontinuous and continuous PM rotor, was attenuated (when compared with speeds close to 500 rpm) and they are approximately the same for both rotors. Hence, it is possible to conclude that the biggest difference, between the discontinuous and continuous PM rotor in terms of oscillations, is the operation in lower angular velocities. The fact that the discontinuous rotor was not able to operate at speeds below 300 rpm, enhances this idea.

By analysing the slips, it is noticeable that for the most of the performed tests the values are high, almost nonsensical in a normal electrical machine. However, it is known that the electrical motor was modified and with the experiments conditions, the motor's air-gap was increased. Such conditions lead to an augmentation of the operation slip. Nevertheless, the slip values can give useful information. Comparing the results of table 3.6, it is observable that the slip associated to the continuous rotor is lower than one verified with the discontinuous rotor. Thus, it is observable that the unstable rotation of the discontinuous PM rotor lead to highest slip values, because the existing torque oscillations due to the intermittent rotation of the discontinuous PM ring works as an extra load torque for the motor. Moreover, it is noticeable that increasing the angular speed, the slip values decreases for both rotors. At 1350 rpm the continuous PM rotor presented a slip value of 10%, which is the value of the three-phase motor slip before the modifications.

3.3.4 Dynamic Analysis

In this section, a dynamic analysis of the system will be done, in order to better understand its dynamic properties and to study the system stabilization. For such purpose, tests will be done, exciting the system radially (Levitation Forces) and axially (Guidance Forces).

Axial dynamics

If the SMB's rotor, when in its stable position inside the rotor, is axially pulled or pushed out, it tends to come back to its stable position in the center of the stator, due to its guidance forces. To analyse this system behavior, a controlled axial displacement was forced and the system response studied.

Fig. 3.35 shows the setup used to acquire the response curve of the system. The rotor D20 was used due to its higher Guidance forces. The stator is displaced onto the point where the guidance forces are maximum, which is around 10 mm, and dropped off, whist the rotor is fixed.

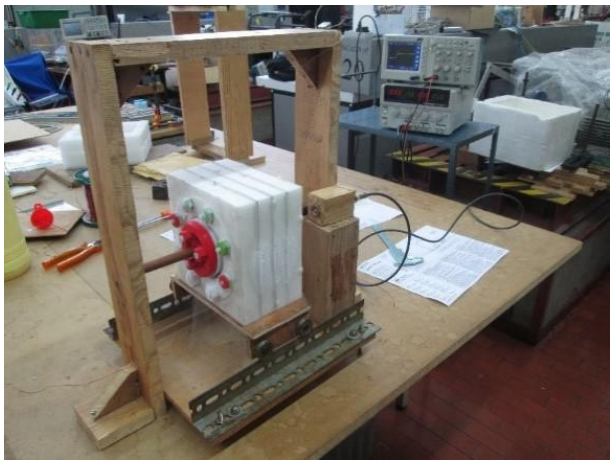

Figure 3.35: Experimental setup used to evaluate the axial dynamics

The position throughout the time is measured by a ultrasonic distance measuring sensor *Baumer* pointed to a stator wall. The sensor specifications and photo are shown in Table 3.7. This sensor was chosen, due to its adequate displacement range. Fig. 3.36 shows the obtained response curve from the oscilloscope.

Table 3.7: Sensor *Baumer UNAM 12U9914/S14D*.

Standard Specifications	
Range Sd	20 to 200 mm
Repeat accuracy	$<$ 0.5 mm
Resolution	$<$ 0.3 mm
Response Time ton	$<$ 30 ms
Temperature Drift	$<$ 2% dist. to target
Sonic frequency	380 kHz
Adjustment	External Teach-in
Alignment Aid	Yellow LED / Red LED

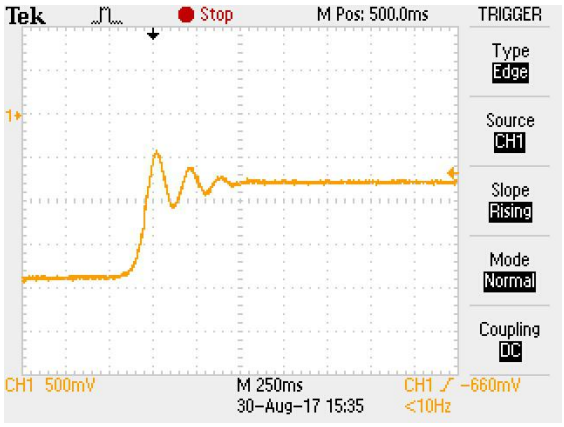

Figure 3.36: Recorded data from the oscilloscope.

The data recorded by the sensor (Volts) was converted to distance by (3.2).

$$Position[mm] = 8.9286U[V] + 16.8 \tag{3.2}$$

Using the *Matlab* application called *System Identification*, the system model was obtained. This *application* calculates a Transfer Function trough an input and an output inserted.

Physically, the system is blocked in a certain position and, when dropped, it is forced to go to a new position, which can be simulated as a *step*. Thus, the used input was a *step* of amplitude 10 (10 mm). The output is the system response. Fig. 3.37 compares the input and output used.

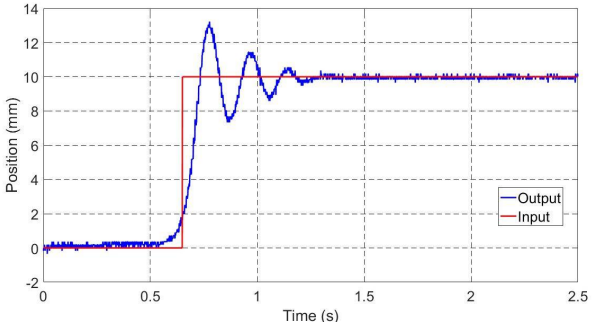

Figure 3.37: Input versus Output used for axial model identification.

The axial dynamics of the system is modelled with a fit level of 70.32% by the transfer function presented in (3.3)

$$G_a(s) = \frac{830.7}{s^2 + 16.81s + 843.5} \tag{3.3}$$

$$\zeta = 0.289; \omega_n = 4.62\,\text{Hz} \tag{3.4}$$

that defines a under damped 2^{rd} order system with damping ratio, $\zeta = 0.289$ and natural frequency, $\omega_n = 4.62$ Hz. A model with a fit level of 88.49% using the transfer function presented in (3.5)

$$G_a(s) = \frac{3.47.10^4}{s^3 + 41.06s^2 + 1365s + 3.495.10^4} \tag{3.5}$$

$$\zeta = 0.133; \omega_n = 5.24\,\text{Hz} \tag{3.6}$$

defines a 3^{rd} order system with damping ratio, $\zeta = 0.133$, natural frequency, $\omega_n = 5.24$ Hz.

Fig. 3.38 shows the obtained curves and the simulated model response using (3.3) and (3.5).

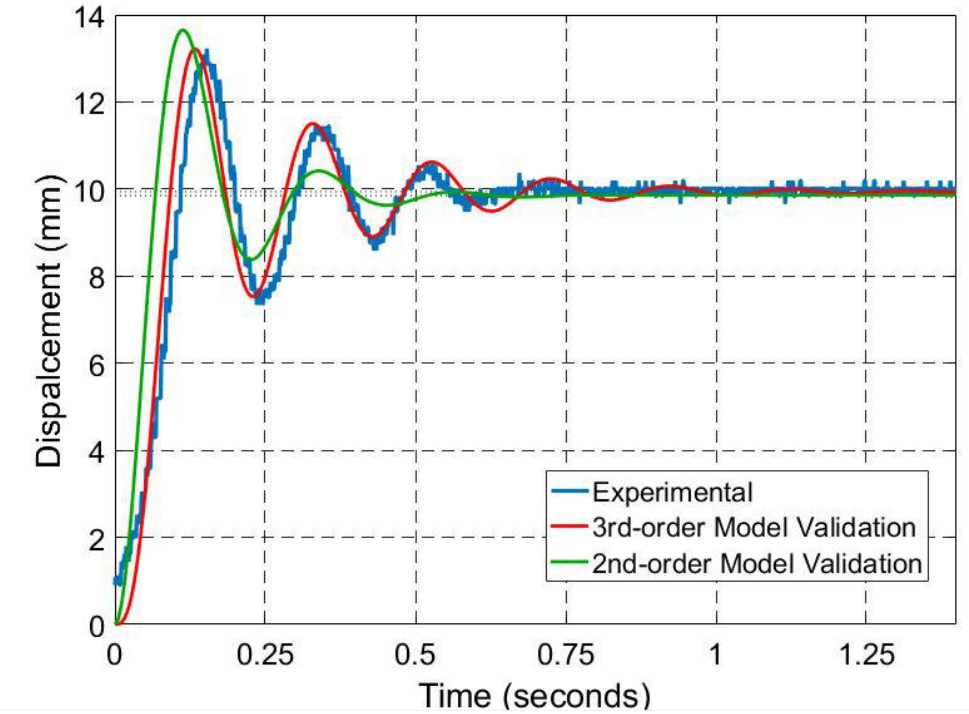

Figure 3.38: Experimental data and model validation for radial system response.

Examining the above, one can see there is pretty good, though not perfect, agreement between the models and the experimental data, namely the 3rd-order model.

Radial dynamics

When excited radially, the rotor's SMB reveals an unstable and uncontrolled behavior. To analyse the SMB radial behavior, the rotor was coupled to a shaft, the same way presented in section 2.3 and section 3.3.3, in order to avoid axial displacements.

Fig. 3.39 shows the setup used to evaluate the radial dynamics of the system. The rotor D5 was used due to its higher levitation forces. The shaft is vertically pushed in the opposite direction of the sensor onto the position where the rotor touches the stator, which is 5 mm. The shaft is dropped off and the position throughout the time is measured by the fiberoptic displacement sensor *PHILTEC, Inc.*, presented in section 3.2.2, pointed to the tube.

Fig. 3.40 shows the obtained response curve from the oscilloscope.

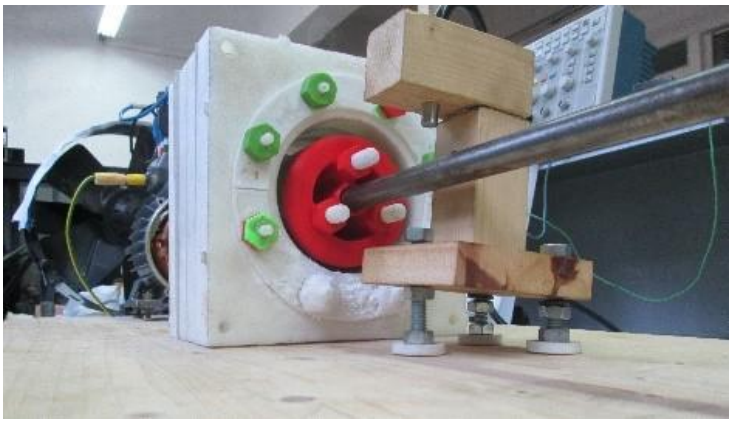

Figure 3.39: Experimental setup used to evaluate the radial dynamics.

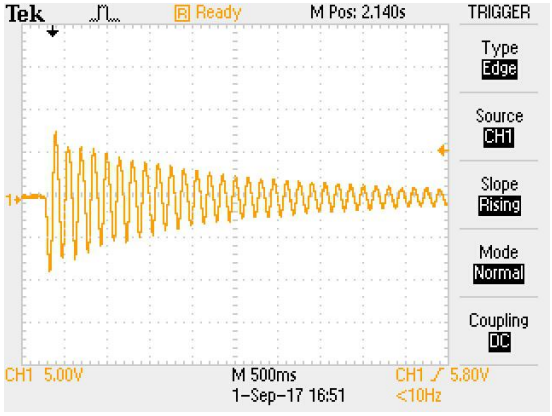

Figure 3.40: Recorded data from the oscilloscope.

The data recorded by the sensor (Volts) was converted to distance by (3.7)

$$Position[mm] = 0.97U[V] \tag{3.7}$$

.

For system identification, the input data was again considered as a step with amplitude of the initial displacement, i.e. the initial position of the shaft, and the output the response of the system, as shown in Fig. 3.41.

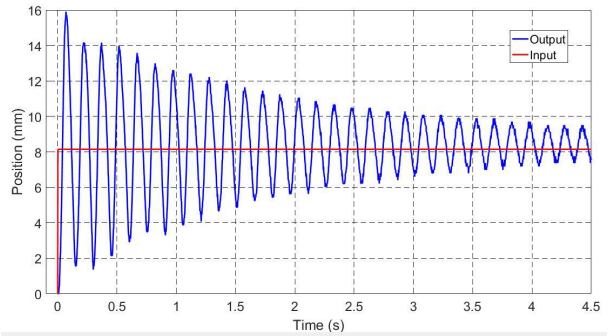

Figure 3.41: Input versus Output used for radial model identification.

The radial dynamics of the system is modelled with a fit level of 83.91%, by the transfer function presented in (3.8)

$$G_a(s) = \frac{1811}{s^2 + 1.1019s + 1746} \tag{3.8}$$

$$\zeta = 0.0122; \omega_n = 6.65\,\text{Hz} \tag{3.9}$$

that defines a under damped 2nd-order system with $\zeta = 0.0.0122$ and $\omega_n = 6.65$ Hz.

Fig. 3.42 shows the displacement of the rotor after conversion and the validation of the model.

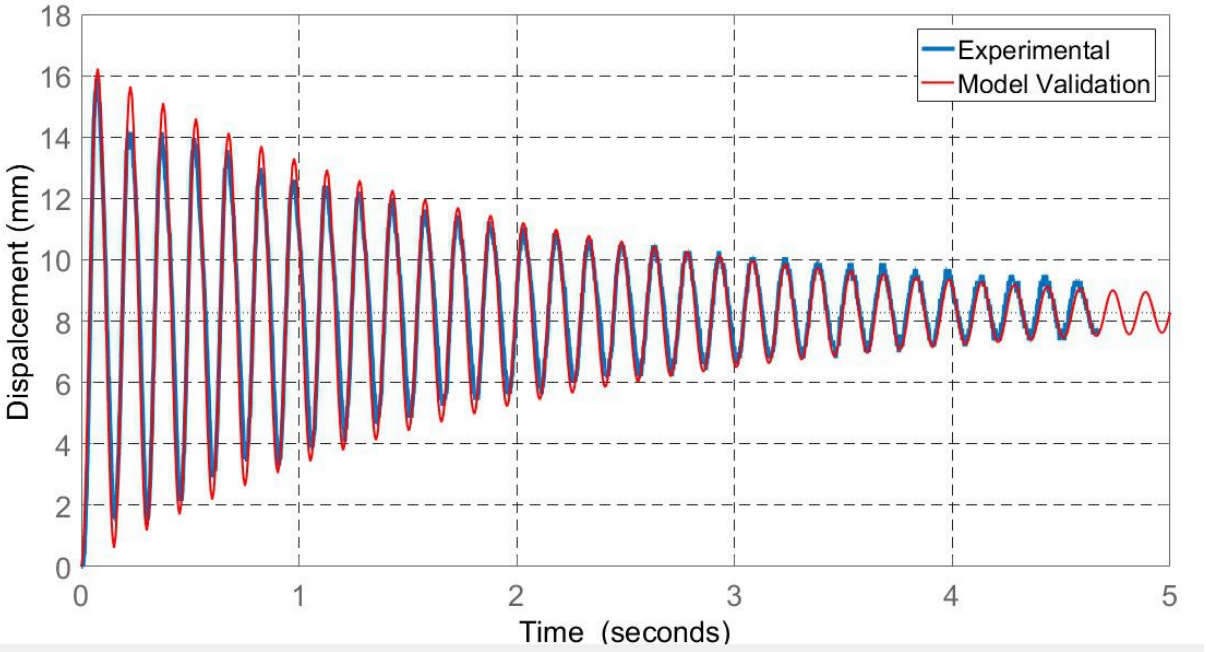

Figure 3.42: Experimental data and model validation for radial system response.

Examining the above, one can see there is pretty good, though not perfect, agreement between the models and the experimental data.

Hence, it is possible to conclude that the axial and radial models of the SMB dynamics can be approximated to linear models with a high level of confidence.

3.3.5 FC Experimental Test

When type-II superconductor bulks are cooled in presence of a magnetic field, known as the FC technique, they trap and memorize that magnetic field. After FC they perform as permanent magnets, generating a magnetic field equal to the trapped one. When they are located in a magnetic field different to the trapped field, they get attracted to a position where the existing field almost equals the trapped field [20].

The objective of the following section is to analyse the differences in terms of forces, using both cooling techniques. Notice that the SMB was conceived to work with ZFC, therefore it is expected that, using the FC procedure, the SMB is not workable.

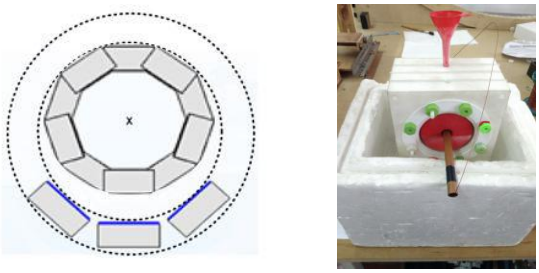

Figure 3.43: FC procedure followed.

The experiment started cooling the superconductor bulks with the rotor placed inside the stator touching on top, as shown in Fig. 3.43. As referred before, the HTS bulks will be attracted to the place where the cooling process happened, however, the own weight of the rotor will push the rotor down. Hence, the farer the cooling position, the higher the repulsive forces between HTSs and PMs, i.e., Levitation Forces. The idea is to trap the magnetic field of the rotor as far as possible, inside the stator, in such a way that Levitation force can compensate the rotor's weight at most.

In this section, the used rotor was always the bulks based PM rotor D5. Hence, the distance between HTS and the rotor operation position is 6.5 mm (stator width and rotor centered air-gap: 4 mm + 2.5 mm), whilst between HTSs and the cooling position is 9 mm (stator width and rotor air-gap: 4 mm + 5 mm). Therefore, the FC is made at a distance of 138.5% from the operation point. The most similar theoretical study is made in [19] for a distance of 150% from the operation point.

Fig. 3.44 shows the SMB, after the FC procedure. As expected, the rotor did not levitate and touched in the bottom instead.

Figure 3.44: SMB after FC procedure.

Fig. 3.45 shows the experimental setups used to measure Levitation and Guidance forces. For measuring Guidance forces the same setup of section 3.24 was used. On the other hand, the setup for Levitation forces was adapted, since these forces were not enough to compensate the rotor weight. Hence, in setup of Fig. 3.45 (a) the difference between the total weight of the rotor and when affected by the magnetic forces inside of the rotor for different eccentricities was measured.

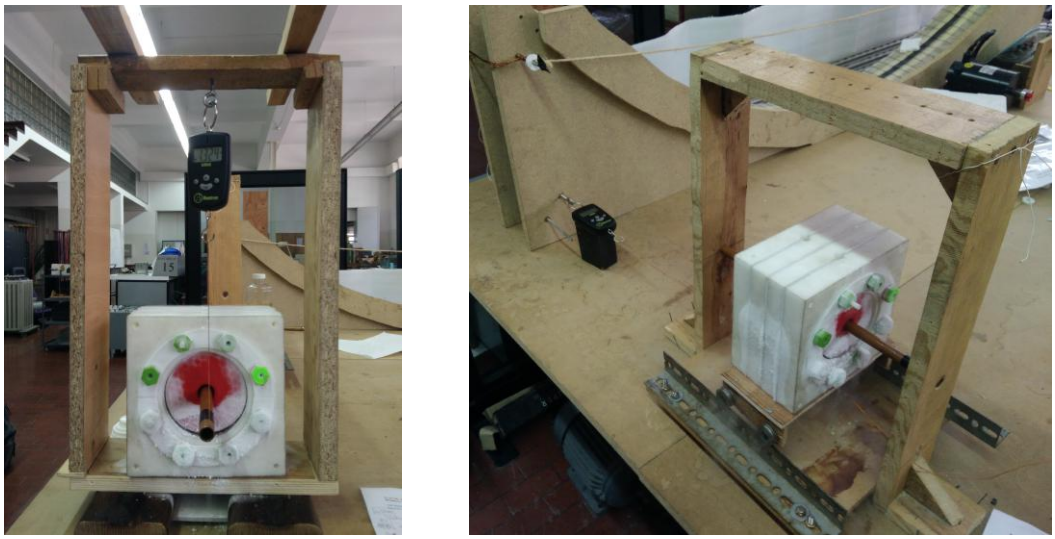

(a) Experimental setup to measure levitation forces.

(b) Experimental setup to measure guidance forces.

Figure 3.45: Experimental setup to measure lifting forces.

Table 3.8 shows the Levitation Forces of discontinuous PM rotor D5 measured using FC. Fig. 3.46 compares results for FC and ZFC using the same rotor. Moreover, the weight of the rotor is plotted, in order to compare with the observed forces.

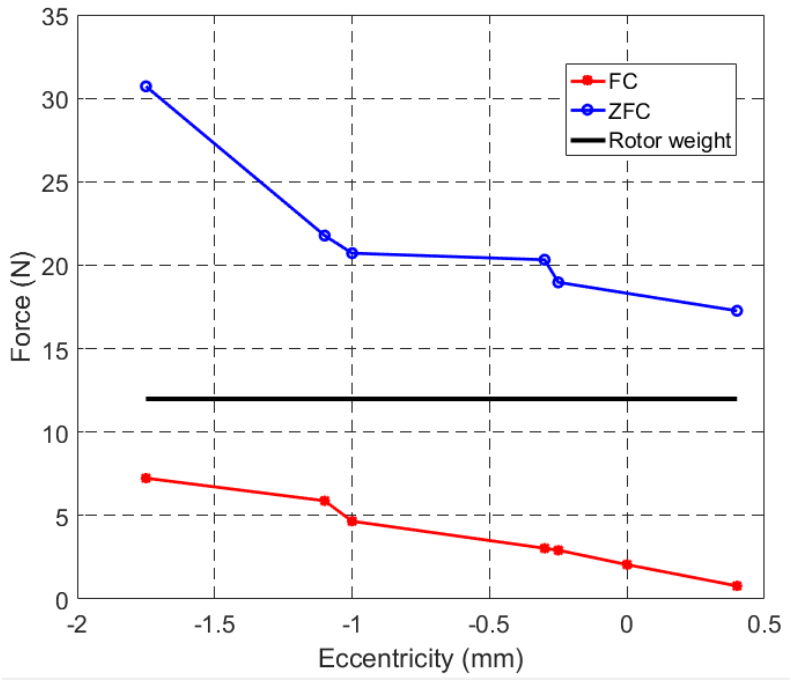

Figure 3.46: Levitation forces comparison using FC and ZFC procedure.

Table 3.8: Measured Levitation Forces for different rotor vertical eccentricities using FC.

Eccentricity (mm)	-1.75	-1.10	-1.00	-0.30	-0.25	0	0.40
Meas. Force (N)	7.24	5.59	4.66	3.04	2.92	2.06	0.78

As observed, the Levitation Forces using FC never outperforms the rotor weight, existing no conditions for levitation.

Table 3.9 shows the measured Guidance forces using FC and Fig. 3.47 compares results for FC and ZFC.

Table 3.9: Measured Guidance Forces for different rotor lateral misalignment using FC.

Eccentricity (mm)	-9	-6	-4	0	4	5	7	8	9	10
Meas. Force (N)	-7.65	-5.59	-3.88	0	2.30	3.51	3.79	5.42	5.28	6.08

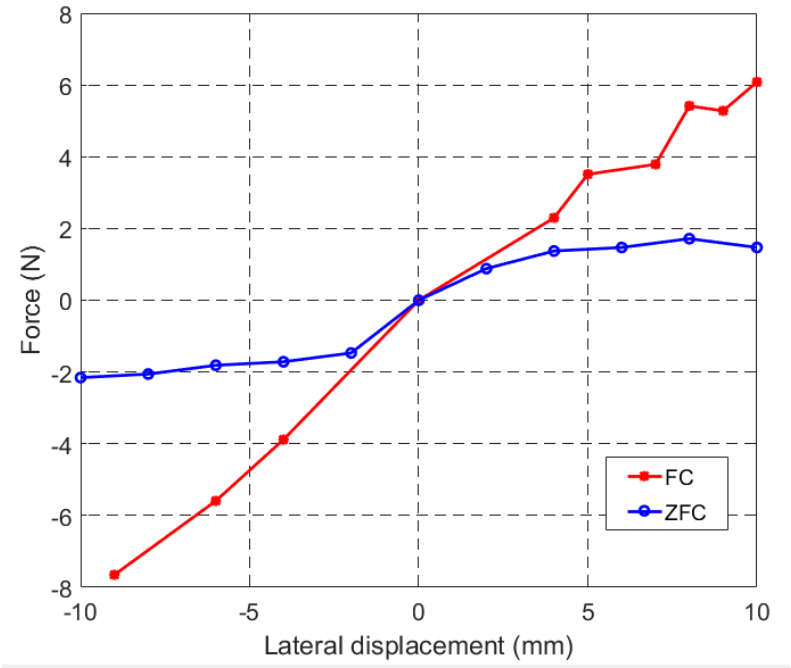

Figure 3.47: Guidance forces comparison using FC and ZFC procedure.

Despite the range of measured displacements for FC is not as big as the ones measured for ZFC, it is possible to conclude that the Guidance forces for FC are quite higher than the observed with ZFC.

Analysing both tests, it is possible to conclude that the SMB is not viable using the FC technique, because the Levitation forces are not enough to support the rotor weight. However, the Guidance forces were substantially higher. A SMB conceived to work with FC could have a better lateral stability.

Chapter 4

Conclusions and Future Work

In this section, the developments on the prototype and the most important conclusions achieved throughout the project are explained. Furthermore, some ideas for future work are suggested and briefly discussed.

4.1 Achievements

In this thesis, a new improved configuration for the horizontal SMB based on ZFC technology was developed. For such purpose, several tools were used to analyse important features, in order to understand the best way to improve them.

A thermal model of the SMB's stator was created to analyse a possible configuration to improve the liquid nitrogen thermal isolation. Trough this model the rate of nitrogen evaporation was predicted. Temperatures and the evaporation rate simulated make are close from the measured experimentally, which validates the model. Furthermore, a new configuration of the SMB's stator was created, in order to decrease the evaporation rate.

A new design of the SMB's rotor was developed, in order to improve its rotation. Actually, using the new rotor based on continuous PMs, the observed equilibrium in the SMB is not obtained in specific angles anymore and the rotor reveals a smooth angular motion instead. Furthermore, when using the setup created in this work, the behaviour analysis of the SMB operating as a bearing for electrical machines concluded that the rotor based on ring PMs reveals advantages, in terms of vibration and slip. Thus, the SMB operating as a real bearing with the new rotor reveals more safety and efficient than the used previously.

A static study of the system was made. Generally, the Levitation and Guidance forces increase using the new rotor, despite its smaller diameter, which allows a more safety configuration for the SMB. The results of simulations and the experiments were approximated. Moreover, it was concluded that adapting the distance between PMs, the SMB can have higher Levitation force or higher lateral stability, according to the requirements.

The dynamics behaviour of the system were also studied, with the focus on the development of a

active stabilizer. Notice that by using sixteen HTS bulks, instead of six used in the present prototype, the dynamics could change, mainly the radial dynamics.

Finally, the viability of the SMB using FC instead of ZFC was studied. The conclusion was that the SMB is not able to operate with the use of the FC technique. However, the Guidance forces have clearly increased.

In general, noticeable advances were achieved by the SMB prototype in order to use it as a viable bearing for electrical machines. Several analyses were made successfully to prove it.

4.2 Future Work

In this section I give some ideas for further works about this project, in order to improve the SMB.

A more effective SMB in terms of Levitation forces and stability could be conceived using sixteen HTS instead of six. The possibility of building the SMB with such configuration might allow interesting improvements.

In this project, the dynamics of the system was studied. Starting from this point, an active control using electromagnetic actuators may be considered in order to improve the stability of the SMB.

Also, the SMB was tested replacing a mechanical bearing of a three-phases motor. An interesting study could be done replacing both mechanical bearings by two SMB as suggested in Fig. 4.1. All the tests developed throughout this work could be also done for this system, namely forces measurement and stability tests.

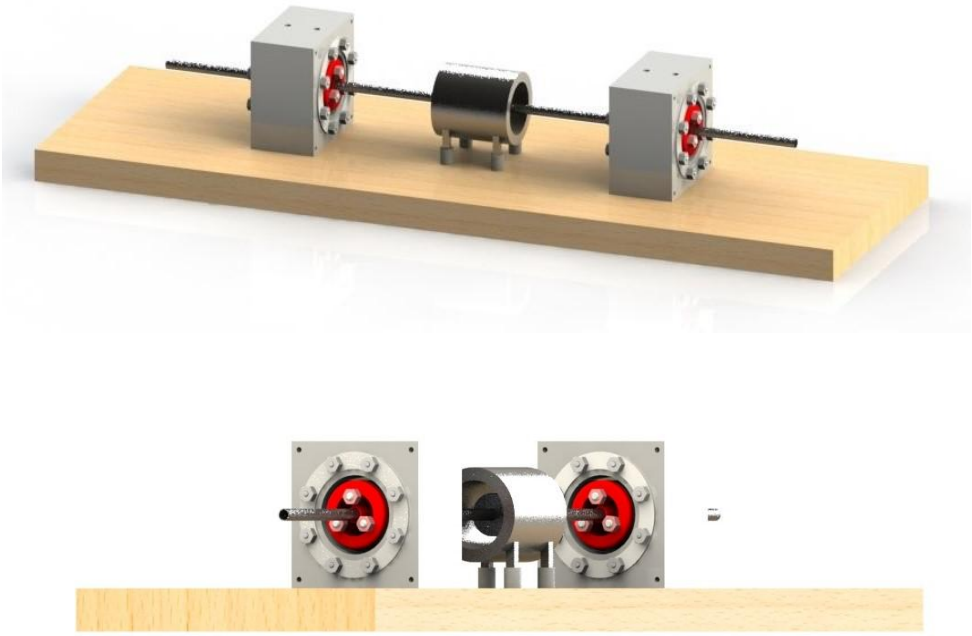

Figure 4.1: SMB replacing both mechanical bearings from a electrical machine.

A study about the thermal fatigue on the stator structure and the HTS bulks may be also done. In fact, the Coffin-Manson expression relates the extension of a structure through the number of cooling and re-heating cycles. From this relation, a FEM analysis may be done to understand the life time expectancy.

As previously referred, the highest energy losses on the SMB are due to the liquid nitrogen evaporation. Thus, a better stator configuration, as well as the choice of a new material, could be very important to achieve a better nitrogen isolation, avoiding its evaporation. A new system with no evaporation should be reached.

Bibliography

[1] M. Carvalho. Levitating bearings using superconductor technology. Master's thesis, Instituto Superior Técnico, Lisboa, 2016.

[2] A. A. Wolfe. Superconductivity and energy conversion: A glimpse into the future. In *Electrical Insulation Conference, 1971 EIC 10th*, pages 208–212. IEEE, 1971.

[3] L. Landau, E. Lifshitz, and L. Pitaevskii. Electrodynamics of continuous media media, 1969.

[4] U. S. Pracht, E. Heintze, C. Clauss, D. Hafner, R. Bek, D. Werner, S. Gelhorn, M. Scheffler, M. Dressel, D. Sherman, et al. Electrodynamics of the superconducting state in ultra-thin films at thz frequencies. *IEEE Transactions on Terahertz Science and Technology*, 3(3):269–280, 2013.

[5] I. Bozovic, J. Eckstein, M. Klausmeier-Brown, and G. Virshup. Superconductivity in epitaxial bi2sr2cuo6/bi2sr2cacu2o8 superlattices: The superconducting behavior of ultrathin cuprate slabs. *journal of Superconductivity*, 5(1):19–23, 1992.

[6] C. Chu. High-temperature superconducting materials: a decade of impressive advancement of t/sub c. *IEEE transactions on applied superconductivity*, 7(2):80–89, 1997.

[7] C. W. Chu. Oxides for high temperature superconductivity and beyond. *Tsinghua Science and Technology*, 3(1):914–935, March 1998.

[8] Cern. Superconductivity. `https://home.cern/about/engineering/superconductivity`. Accessed: 2017-08-07.

[9] Wikipedia, the free encyclopedia. bearing (mechanical). [online]. `https://en.wikipedia.org/wiki/Bearing_(mechanical)`. Accessed: 2017-08-07.

[10] Abma, american bearing manufacturing association. what are bearings?.[online]. `https://www.americanbearings.org/?page=what_are_bearings`. Accessed: 2017-08-07.

[11] SKF. Cracks. `http://www.skf.com/cn/en/products/bearings-units-housings/roller-bearings/principles/troubleshooting/bearing-failures-and-their-causes/bearing-damage/cracks/index.html`. Accessed: 2017-09-21.

[12] SKF. Bearings that save energy. `http://evolution.skf.com/us/beast3/`. Accessed: 2017-09-21.

[13] J. G. Bitterly. Flywheel technology: past, present, and 21st century projections. *IEEE Aerospace and Electronic Systems Magazine*, 13(8):13–16, 1998.

[14] C. Tshizubu and J. A. Santisteban. A simple pid controller for a magnetic bearing with four poles and interconnected magnetic flux. In *Advanced Control of Industrial Processes (AdCONIP), 2017 6th International Symposium on*, pages 430–435. IEEE, 2017.

[15] R. Duffin. Free suspension and earnshaw's theorem. *Archive for Rational Mechanics and Analysis*, 14(1):261–263, 1963.

[16] B. Bolund, H. Bernhoff, and M. Leijon. Flywheel energy and power storage systems. *Renewable and Sustainable Energy Reviews*, 11(2):235–258, 2007.

[17] F. Werfel, U. Floegel-Delor, R. Rothfeld, T. Riedel, B. Goebel, D. Wippich, and P. Schirrmeister. Superconductor bearings, flywheels and transportation. *Superconductor Science and Technology*, 25(1):014007, 2011.

[18] A. Arsénio, M. Carvalho, C. Cardeira, P. C. Branco, and R. Melício. Conception of a ybco superconducting zfc-magnetic bearing virtual prototype. In *: Proocedings of the IEEE 17th International on Power Electronics and Motion - PEMC 2016*, pages 1226–1230, Varna, Bulgaria, 25-30 September 2016.

[19] A. Arsénio, M. Carvalho, C. Cardeira, P. C. Branco, and R. Melício. Viability of a frictionless bearing with permanent magnets and hts bulks. In *: Poocedings of the IEEE 17th International Conference on Power Electronics and Motion Control - PEMC 2016*, pages 1231–1236, Varna, Bulgaria, 2016.

[20] A. J. Arsénio, M. V. Carvalho, C. Cardeira, R. Melício, and P. J. C. Branco. Experimental setup and efficiency evaluation of zero-field-cooled (zfc) ybco magnetic bearings. *IEEE Transactions on Applied Superconductivity*, 27(4):1–5, 2017.

[21] M. Sparing, A. Berger, F. Wall, V. Lux, S. Hameister, D. Berger, M. Hossain, A. Abdkader, G. Fuchs, C. Cherif, et al. Dynamics of rotating superconducting magnetic bearings in ring spinning. *IEEE Transactions on Applied Superconductivity*, 26(3):1–4, 2016.

[22] S. Sivrioglu, S. Basaran, and A. S. Yildiz. Multisurface hts-pm levitation for a flywheel system. *IEEE Transactions on Applied Superconductivity*, 26(8):1–6, 2016.

[23] Z. Yu, G. Zhang, Q. Qiu, L. Hu, B. Zhuang, and M. Qiu. Analyses and tests of hts bearing for flywheel energy system. *IEEE Transactions on Applied Superconductivity*, 24(3):1–5, 2014.

[24] W. Liu, D. Kang, C. Zhang, G. Peng, X. Yang, and S. Wang. Design of a high- tc superconductive maglev flywheel system at 100-kw level. *IEEE Transactions on Applied Superconductivity*, 26(4): 1–5, 2016.

[25] S. Sivrioglu and S. Basaran. A dynamical stiffness evaluation model for a ring-shaped superconductor magnetic bearing system. *IEEE Transactions on Applied Superconductivity*, 25(4):1–7, 2015.

[26] S. Sakai, K. Oguni, and S. Ohashi. Effect of the magnetic configuration on the rotational motion in the attractive-type hts-permanent magnet hybrid bearing. *IEEE Transactions on Applied Superconductivity*, 26(4):1–4, 2016.

[27] H. Walter, J. Bock, C. Frohne, K. Schippl, H. May, W. Canders, P. Kummeth, W. Nick, and H. Neumueller. First heavy load bearing for industrial application with shaft loads up to 10 kn. In *Journal of Physics: Conference Series*, volume 43, page 995. IOP Publishing, 2006.

[28] evico. Industrial superconductor bearings. `http://www.evico.de/en/magnetic-bearings/industrial-superconductor-bearings/`. Accessed: 2017-08-11.

[29] can superconductors. Superconducting magnetic bearings - supplied in coooperation with magsoar. `http://www.can-superconductors.com/superconducting-magnetic-bearings.html/`. Accessed: 2017-10-02.

[30] P. da Costa Branco and J. Dente. Design and experiment of a new maglev design using zero-field-cooled ybco superconductors. *IEEE Transactions on Industrial Electronics*, 59(11):4120–4127, 2012.

[31] J. Fernandes, I. Montes, R. Sousa, C. Cardeira, and P. C. Branco. Superconductor joule losses in the zero-field-cooled maglev vehicle. *IEEE Transactions on Applied Superconductivity*, 26(3):1–7, 2016.

[32] M. V. Carvalho, A. J. Arsenio, C. Cardeira, P. J. C. Branco, and R. Melício. Levitating bearings using superconductor technology under smart systems scope. In *: Technological Innovation for Smart Systems*, pages 390–397, May 2017.

[33] A. Arsénio, M. Roque, C. Cardeira, P. C. Branco, and R. Melício. Prototype of a rings based zero-field-cooling (zfc) ybco magnetic bearing. In *: Proocedings of the 16th European Conference on Appllied Superconductivity EUCAS2017*, Geneva, Switzerland, 17-22 September 2017.

[34] T. L. Bergman and F. P. Incropera. *Fundamentals of heat and mass transfer*. John Wiley & Sons, 2011.

[35] J. Mais. *Spectrum Analysis: The Key Features of Analyzing Spectra.* SKF USA Inc., 2002.